

Downscaling ocean conditions with application to the Gulf of Maine, Scotian Shelf and adjacent deep ocean



Anna Katavouta*, Keith R. Thompson

Department of Oceanography, Dalhousie University, Halifax, Nova Scotia, Canada

ARTICLE INFO

Article history:

Received 1 December 2015

Revised 17 April 2016

Accepted 22 May 2016

Available online 24 May 2016

Keywords:

Dynamical downscaling

Regional ocean model

One-way nesting

Spectral nudging

Northwest Atlantic and shelf seas

ABSTRACT

The overall goal is to downscale ocean conditions predicted by an existing global prediction system and evaluate the results using observations from the Gulf of Maine, Scotian Shelf and adjacent deep ocean. The first step is to develop a one-way nested regional model and evaluate its predictions using observations from multiple sources including satellite-borne sensors of surface temperature and sea level, CTDs, Argo floats and moored current meters. It is shown that the regional model predicts more realistic fields than the global system on the shelf because it has higher resolution and includes tides that are absent from the global system. However, in deep water the regional model misplaces deep ocean eddies and meanders associated with the Gulf Stream. This is not because the regional model's dynamics are flawed but rather is the result of internally generated variability in deep water that leads to decoupling of the regional model from the global system. To overcome this problem, the next step is to spectrally nudge the regional model to the large scales (length scales > 90 km) of the global system. It is shown this leads to more realistic predictions off the shelf. Wavenumber spectra show that even though spectral nudging constrains the large scales, it does not suppress the variability on small scales; on the contrary, it favours the formation of eddies with length scales below the cutoff wavelength of the spectral nudging.

© 2016 The Author(s). Published by Elsevier Ltd.

This is an open access article under the CC BY-NC-ND license.

(<http://creativecommons.org/licenses/by-nc-nd/4.0/>)

1. Introduction

The present generation of data-assimilative ocean models is capable of realistic eddy resolving simulations of the global ocean and interactions with other components of the climate system (e.g., atmosphere, sea ice). Two well known examples of the new generation of operational ocean systems with global domains and relatively high resolution are the US Naval Oceanographic Office 1/12° system based on the HYbrid Coordinate Model (HYCOM, Chassignet et al., 2009) and the 1/12° MERCATOR system based on the Nucleus for European Modelling Ocean framework (NEMO, Molines et al., 2014).

Despite these recent advances in the development of global ocean forecast systems, many practical applications (e.g., calculating the probability of extreme events, forecasting oil spill trajectories, supporting marine search and rescue, interpreting the movement of tagged marine animals) require information on smaller spatial scales. The need for higher resolution can be particularly acute on continental shelves where variability on scales of sev-

eral km and less can be of practical importance. However, regional ocean conditions are often controlled by processes operating on large scales, e.g., western intensification of boundary currents, propagating Rossby waves. This leads to the need for downscaling to help estimate local and regional features from coarser scale patterns. Ocean modellers are responding to this need by developing unstructured grid and nested structured grid models with higher resolution reserved for regions of primary interest (i.e., dynamical downscaling, see Blayo and Debreu, 2006, for an overview of the ocean nesting problem).

The atmospheric modelling community has considerable experience in dynamical downscaling and the specification of lateral open boundary conditions for nested high resolution models. Many studies have examined the accuracy of one-way nesting (e.g., de Elia et al., 2002; Denis et al., 2002; Laprise, 2003; Nutter et al., 2004). In general, one-way nesting is challenging because of i) internally generated variability in the regional model that may lead to decoupling of the regional model solution from the large scale fields used to drive it (e.g., Giorgi and Bi, 2000; Caya and Biner, 2004; Rinke et al., 2004; Alexandru et al., 2009; Laprise et al., 2012) and, ii) practical difficulties in the specification of lateral open boundary conditions (e.g., sponge layers, Davies, 1976). Similar problems have been noted by the ocean modelling community

* Corresponding author.

E-mail addresses: a.katavouta@dal.ca (A. Katavouta), keith.thompson@dal.ca (K.R. Thompson).

(e.g., Marchesiello et al., 2001). To constrain atmospheric internal variability, and overcome the impact of ill-posed lateral open boundary conditions, a method referred to as spectral nudging has been proposed (Waldron et al., 1996; von Storch et al., 2000). According to this method, the large scales of the regional model are nudged towards independent estimates of the true large scales (estimated from, for example, a coarser resolution global system or a reanalysis) and the small scales are left to evolve freely according to the regional model's dynamics.

Spectral nudging is based on the idea that the large scales may be used to guide the reconstruction and prediction of the small scales. (See Appendix A for the relationship between frequency dependent and spectral nudging.) In an independent study based on a similar idea, Henshaw et al., 2003 showed that small scale modes of variability of the solutions to the unforced Navier–Stokes and Burger's equations can be recovered with surprising accuracy from the time history of a few of the large scale modes, due to their nonlinear coupling. Katavouta and Thompson (2013) extended the analysis of Henshaw et al. (2003) to a flow regime that approximates the real ocean using an ocean quasi-geostrophic model. They showed that important features of the ocean circulation, including the positions of a meandering mid-ocean jet and the associated pinch-off eddies, can be recovered from the time history of a small number of large scale modes. This result is significant because it implies that even though the atmosphere and ocean have important differences (e.g., the ocean's internal Rossby radius of deformation is typically 100 times smaller than that of the mid-latitude atmosphere, coastal boundaries have a major impact on ocean circulation), spectral nudging of realistic ocean models may also be effective due to the shared nonlinearity of the governing equations.

As a follow-up to Katavouta and Thompson (2013), we now check if the skill of a realistic regional ocean model can be improved by assimilating information on the large scales. The focus of the present study is on downscaling only information on the large scales; we do not consider the benefit of assimilating observations directly into the regional model. This means that the present study is relevant to applications for which the number of observations can be very low or even zero. For example, the present study is relevant to i) downscaling global climate change scenarios for which no observations will be available, ii) downscaling global and basin scale ocean hindcasts for the last 50 years for which time the availability of observations will be limited, and iii) using a rapidly relocatable ocean model to predict conditions for an arbitrary area (e.g., a small coastal bay, part of the shelf or shelf break) undergoing a marine emergency and with an uncertain number of observations. The difficulties and benefits of assimilating observations into the regional model are discussed in the final section.

As a case study we focus on downscaling ocean conditions from a well known global system (the US Naval Oceanographic office 1/12° assimilative system based on HYCOM) to the Gulf of Maine, Scotian Shelf and adjacent North Atlantic. We first construct a one-way nested regional model, based on the NEMO modelling framework, in order to identify the limitations of the global system on the shelf. The regional model is evaluated using a range of observations, and challenges unique to ocean downscaling are identified. For example, the regional model includes both shelf and deep water and thus covers environments with significantly different processes, and spatial and temporal scales. As will become clear, this means the regional model may predict more realistic fields than the global system on the shelf, but less accurate fields in deep water due to the problems associated with one-way nesting described above. To overcome this problem, we then spectrally nudge the regional model to the large scales predicted by the global system.

The outline of this paper is as follows. The global and regional ocean models, the spectral nudging methodology modified for realistic ocean applications, and the design of the numerical experi-

Table 1
Main characteristics of the global system, GoMSS and GoMSS+.

	Global system	GoMSS	GoMSS+
Model Framework	HYCOM	NEMO	NEMO
Resolution	1/12°	1/36°	1/36°
Domain	Global	Gulf of Maine, Scotian Shelf, and adjacent deep ocean	Gulf of Maine Scotian Shelf, and adjacent deep ocean
Atmospheric forcing	NOGAPS	CFSR	CFSR
Tidal forcing	No	FES2004	FES2004
Assimilation	NCODA	No	Spectral nudging

ments, are described in Section 2. In Section 3 the performance of the one-way nested version of the regional model is evaluated and discussed. The improvements resulting from the spectral nudging are discussed in Section 4. In Section 5 we estimate wave-number spectra of predictions by the three models (global, one-way nested and spectrally nudged) and examine the impact of spectral nudging on the small scales that are not directly influenced by spectral nudging. The main results of the study, and their implications, are summarized in Section 6. Note on terminology: we subsequently use “model predictions” in the generic sense (i.e., in the same way a regression model predicts y from x) and not in the sense of forecasting (i.e., predicting the future).

2. Methods

A brief description is given below of the global system and the higher resolution regional model. The period of integration of the regional model is 2010–2012. The spectral nudging method is then described. The characteristics of each system are summarized in Table 1.

2.1. Global system

The fields to be downscaled are obtained from the HYCOM+NCODA global 1/12° analysis system. These fields are provided by the HYCOM Consortium (www.HYCOM.org). NCODA (Navy Coupled Ocean Data Assimilation) refers to the assimilation scheme used in the global system. The global system has a horizontal resolution of 1/12° in both longitude and latitude (about 7 km at mid-latitudes and 3.5 km at the poles). Daily snapshots from the global system are available for 32 vertical z -levels. The surface atmospheric forcing comes from the 3-hourly Navy Operational Global Prediction System (NOGAPS) with a 1/2° resolution. A simple thermodynamic ice model is used that includes ice formation and melting but no ice motion. For further details about the global system's physics and configuration see Bleck (2002) and Chassignet et al. (2007); (2009).

The global system assimilates along track altimeter observations, sea surface temperature observed by satellites, sea ice concentration from the special sensor microwave/imager (SSM/I), and in-situ vertical profiles of temperature and salinity from various platforms (e.g., Argo floats, ships, moored buoys). The analysis updates sea ice concentration, salinity, temperature, dynamic height and velocity. The assimilation is performed using multivariate optimum interpolation (Cummins, 2005; Cummins and Smedstad, 2013). The currents are updated based on multivariate correlations between velocity and dynamic height, and the altimeters' sea surface height observations are vertically projected using synthetic temperature and salinity profiles from the Modular Ocean Data Assimilation System (Fox et al., 2002).

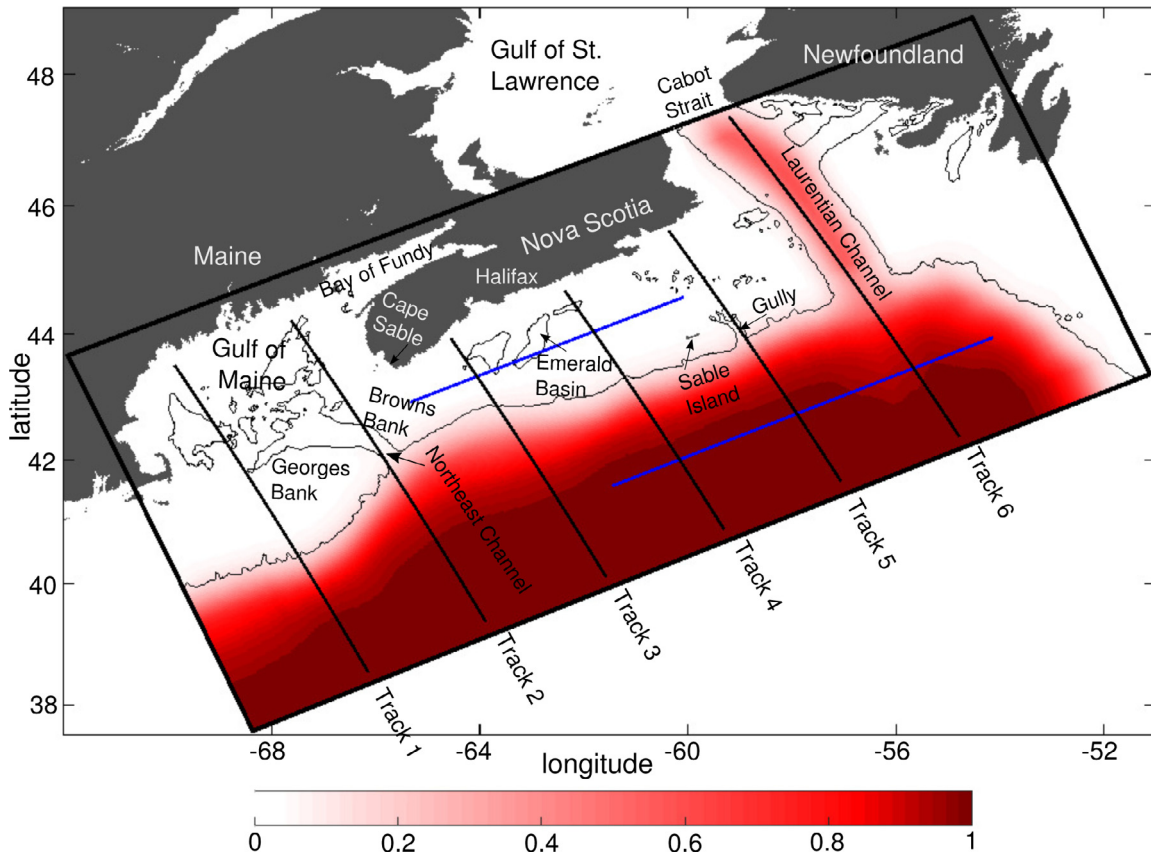


Fig. 1. The GoMSS model domain (box defined by the black lines), with major bathymetric features, place names and the horizontal variation of γ (i.e., $\phi(x, y)$, see (5)) defined by the colorbar. The thin black line shows the 200 m isobath. The black lines labelled Track 1 to 6 define the altimeter tracks. The blue lines (one on the shelf and one in deep water) define the lines along which wavenumber spectra are estimated. Note that the southern Gulf of St. Lawrence is not represented in the regional model and has been masked out. (For interpretation of the references to colour in this figure legend, the reader is referred to the web version of this article.)

2.2. Regional model

The regional model is based on the ocean component (Ocean Parallelise System, [Madec et al., 1998](#)) of the Nucleus for European Modelling of the Ocean (NEMO) version 3.1 framework ([Madec, 2008](#)). The model domain covers the Gulf of Maine, Scotian Shelf and adjacent deep ocean ([Fig. 1](#)). Henceforth the regional model in the one-way nesting set-up is referred to as GoMSS. It has a horizontal resolution of approximately $1/36^\circ$ in longitude and latitude (2.8 km average grid spacing) and 52 z-levels with a spacing that varies from 0.7 m closest to the surface to 233 m for the deepest level (4000 m). All depths exceeding 4000 m were set to this value (i.e., clipped). A barotropic-baroclinic time split approach is used to solve separately for the fast (barotropic) motions and the slower (baroclinic) motions. The barotropic and baroclinic time steps are 6 s and 180 s respectively.

Six atmospheric variables from the global NCEP climate forecast system reanalysis (CFSR, [Saha et al., 2010](#)) are used to force the model at the atmosphere-ocean interface: wind at 10 m above the ocean surface, air temperature and humidity at 2 m, precipitation, and longwave and incoming shortwave radiation. The reanalysis fields have a time spacing of 6 hours and a horizontal resolution of approximately 0.3° .

The model's initial and lateral open boundary conditions for temperature, salinity, sea surface height and velocity are specified using predictions from the global system extracted daily. Five tidal constituents (M_2 , N_2 , S_2 , K_1 , O_1) are also used to drive the model along its lateral open boundaries. (The global system does not include tides.) Tidal elevation and transport were obtained from

the FES2004 barotropic global tidal model ([Lyard et al., 2006](#)). A Flather radiation scheme ([Flather, 1976](#)), based on prescribed normal flow and sea surface height, is used for the barotropic currents normal to the open boundaries. A radiation relaxation type algorithm (Orlanski forward implicit, [Marchesiello et al., 2001](#)) with a 10 grid point sponge layer is used for the baroclinic currents. (The barotropic currents are estimated by vertical averaging the global system fields and then adding the contribution from the tides.) Temperature and salinity within GoMSS's sponge layer are set to the global system values when flow enters the domain and a simple upwind advection scheme is used when the flow leaves the domain. For further details about the model's physics see [Katavouta et al. \(2015\)](#).

2.3. Spectral nudging

The basic idea is to additionally force the model over its interior using large scales from the global system. Henceforth the regional model with spectral nudging is referred to as GoMSS⁺. In this study two variables are updated directly by spectral nudging: temperature and salinity. Following [Katavouta and Thompson \(2013\)](#) we write the discretized salinity and temperature equations in the form

$$T_t = \mathcal{D}_t(T_{t-1}) + \gamma \langle T_t^{GS} - \mathcal{D}_t(T_{t-1}) \rangle_L \quad (1)$$

$$S_t = \mathcal{D}_t(S_{t-1}) + \gamma \langle S_t^{GS} - \mathcal{D}_t(S_{t-1}) \rangle_L \quad (2)$$

where T_t and S_t are the model temperature and salinity state vectors at time t (with each element corresponding a specific model

Table 2
Spectral nudging parameters.

Parameter	Value
Number of Butterworth filter passes	10
Cutoff wavelength, λ_c	90 km
Nudging time step	12 minutes
Relaxation time	1 h
Overall nudging strength, γ_0	0.2
Width of transition zone, Δh	1200 m
Transition depth, h_0 :	
Laurentian Channel	350 m
Elsewhere	2000 m

grid point), \mathcal{D}_t is a nonlinear operator representing the model's dynamics and forcing, T^{GS} and S^{GS} are the temperature and salinity fields from the global system, γ is the nudging coefficient and $\langle \cdot \rangle_L$ denotes a quantity that has been spatially smoothed to extract its large scale component. The same γ is used for salinity and temperature. According to the above updating equations, only the large scales are nudged and the small scales evolve freely according to the dynamics and forcing of GoMSS.

To obtain the large scale component (Katavouta and Thompson, 2013) used two dimensional Fourier transforms. This approach is commonly used in atmospheric regional models and simple rectangular model domains. For the real ocean the complexity of the coastline prohibits the use of Fourier transforms. To spatially smooth the temperature and salinity nudges (i.e., evaluate $\langle \cdot \rangle_L$) we used 10 passes of a two dimensional recursive low-pass, second order Butterworth filter (similar to Thompson et al., 2006). The nudges over land were reset to zero after each pass of the filter.

The parameter choices for the Butterworth filter and γ are listed in Table 2. The Butterworth filter cutoff wavelength (λ_c) was set equal to 90 km, which is about three times larger than the first baroclinic Rossby radius of deformation over the model domain. This choice of λ_c was based on sensitivity experiments that ensured spectral nudging does not suppress variability on eddy and smaller scales.

The nudging parameter γ varies with horizontal and vertical position as follows

$$\gamma = \gamma_0 \Gamma(x, y, z) \quad (3)$$

where $\Gamma(x, y, z)$ is a function of position and γ_0 is a constant that can be interpreted as the ratio of the nudging time step divided by the nudging relaxation time scale. The nudging time step is set equal to 12 minutes, corresponding to four baroclinic time steps. The value of the relaxation time scale depends on the application and we chose it based on sensitivity experiments. Because the purpose of this study is to show that spectral nudging can address weaknesses in the one-way nesting method, we decided to apply relatively strong nudging and used a relaxation time of one hour leading to $\gamma_0 = 0.2$. Note that similar results were obtained for $0.05 < \gamma_0 < 1$.

As will become clear in Section 3, the differences between GoMSS and the global system are largest in deep water. Additionally, GoMSS is more realistic than the global system on the shelf because it includes tides and has higher resolution. For these reasons, we decided to apply spectral nudging only in the deep water and made $\Gamma(x, y, z)$ a function of bathymetry. Furthermore, the realism of the global system's temperature and salinity fields is expected to be higher near the surface where there are relatively more observations available for assimilation. These considerations led to the following form for $\Gamma(x, y, z)$:

$$\Gamma(x, y, z) = \phi(x, y) \left[1 - \frac{z}{h_{\max}} \right]^{\frac{1}{4}} \quad (4)$$

$$\phi(x, y) = \frac{1}{2} \left[1 + \tanh \left(\frac{h - h_0}{\Delta h} \right) \right] \quad (5)$$

where z denotes model depth, $h(x, y)$ and h_{\max} are the regional model bathymetry and its maximum value (4000 m) respectively, and h_0 is the transition depth (set equal to 2000 m, except along the Laurentian Channel where $h_0 = 350$ m). The parameter Δh controls the rapidity of the transition from no nudging to nudging as water depth increases. We set Δh equal to 1200 m. To smooth variations of γ in the horizontal, the regional model bathymetry used in (5) was smoothed using a central moving average filter with a 100 km spatial window. The horizontal variation of Γ , i.e., $\phi(x, y)$, is shown in Fig. 1.

3. Strengths and weaknesses of global system and GoMSS

The global system has been extensively evaluated by comparison with observations (e.g., Chassignet et al., 2009; Metzger et al., 2008) and shown to be capable of providing accurate predictions of temperature, salinity, sea level, currents and the position of mid-ocean jets and associated eddies and meanders. However, as noted in the Introduction, higher resolution and the explicit representation of tides (missing from the global system) may be required for several important coastal applications.

GoMSS has been designed to address the above weaknesses of the global system through increased model resolution and the inclusion of tides which are known to be important in the Gulf of Maine and on the Scotian Shelf. In a recent study Katavouta et al. (2015) showed that the tides and their seasonal variability are well represented in GoMSS. It was also shown that GoMSS can reproduce important features caused by the interaction of water density, bathymetry and the tides. For example it was shown that the model generates strong currents that can exceed 0.2 m s^{-1} around shallow features like Georges Bank and Browns Bank due to tidal rectification and the density fronts that arise due to the intense tidal mixing in the shallow water. Note on terminology: we use "tidal rectification" to refer to the mean currents caused by the nonlinear advection terms in the horizontal momentum equation (e.g., Loder, 1980).

To investigate if GoMSS improves the global system's predictions of temperature, salinity, sea level and current, we now compare both of them with observations.

3.1. Temperature and Salinity

The hydrographic fields predicted by the global system and GoMSS have been compared to sea surface temperature observations from satellites and observed vertical profiles of temperature and salinity. The sea surface temperature observations are in the form of daily Moderate Resolution Imaging Spectroradiometer (MODIS) data at 4.6 km resolution downloaded from the NASA OceanColor website (http://dx.doi.org/10.5067/Terra/MODIS_OC.2014.0 and http://dx.doi.org/10.5067/Aqua/MODIS_OC.2014.0). The vertical profiles of temperature and salinity were obtained from i) CTDs deployed on the shelf and ii) Argo floats in deep water. The horizontal locations of all profiles are shown in Fig. 2. The CTD data were obtained from the World Ocean Database 2013 (WOD13, Boyer et al., 2013) and the Argo float data from the Global Data Assembly Centre (<http://dx.doi.org/10.12770/1282383d-9b35-4eaa-a9d6-4b0c24c0cfc9>).

Sea surface temperature: The top panels of Fig. 3 show snapshots of surface temperature from satellite observations, the global system and GoMSS for 22-July 2012. This date was selected because of the relatively good satellite coverage; similar results were obtained for different dates. A more quantitative comparison is shown in the bottom panel of Fig. 3 where time variations of sea

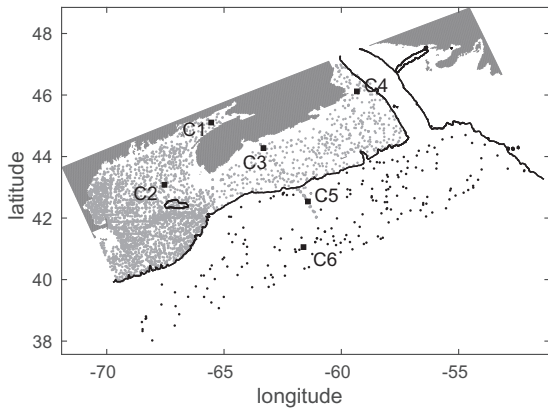


Fig. 2. Locations of the observed CTD (gray dots) and Argo (black dots) profiles of temperature and salinity for 2010–2012. The squares (labelled C1 to C6) mark the locations of the temperature and salinity profiles shown in Figs. B.1 and B.2. The black line is the 300 m isobath.

surface temperature predicted by GoMSS and the global system at a deep water location are compared with co-located observations. The fit is summarized in Table 3. The global system has small bias and the standard deviation of the differences is 1.85°C. Overall, the sea surface temperatures predicted by the global system are consistent with the satellite observations in the deep water. This is to be expected because the global system assimilates these observations. However, the upper panels of Fig. 3, and similar comparisons for other dates (not shown), indicate that the global system differs from the observations on the shelf, particularly in regions with strong mixing caused by vigorous tidal currents (e.g., Gulf of Maine).

On the shelf, GoMSS provides more accurate predictions of surface temperature than the global system at locations where tides are known to have a significant effect on the density field, e.g., Gulf of Maine, Bay of Fundy, Georges Bank (see Fig. 3). More quantitatively, Table 3 shows the global system and GoMSS have neg-

Table 3

Mean and standard deviation of the difference between the observed and predicted time series of daily sea surface temperature, 2010–2012. The first and second rows correspond to a location in the deep water (shown by the black star in Fig. 3). The third and fourth rows correspond to a location on the shelf (shown by the black circle in Fig. 3). All values are in °C.

	Global system	GoMSS	GoMSS ⁺
		Deep water	
Mean	-0.64	-0.24	-0.71
Standard deviation	1.85	2.82	1.77
		Shelf	
Mean	-0.67	-0.56	-0.55
Standard deviation	1.51	1.39	1.38

ligible bias at a representative shelf location but GoMSS has a smaller time-varying deviations about the observations than the global system. The situation is reversed in deep water and GoMSS predictions of surface temperature are much less accurate than those of the global system. For example, Fig. 3 clearly shows that GoMSS misplaces the front between the warm slope water and the cold shelf water, and the position of several eddies and meanders. Table 3 also shows that, similar to the global system, GoMSS has negligible bias at the representative deep water location but the standard deviation of the errors is 2.82°C, approximately 50% higher than the corresponding value for the global system.

Vertical profiles of temperature and salinity: A detailed comparison of observed and predicted vertical profiles for six representative locations (C1 to C6 in Fig. 2) is given in Appendix B. It is shown that, on the shelf, GoMSS gives more accurate predictions of mixed layer depth, and the shape of the thermocline and halocline, than the global system. In deep water the global system predicts temperature and salinity profiles more accurately than GoMSS.

To quantify the agreement between the observed and predicted profiles, the temperature and salinity bias, and the standard deviation of the difference between observations and predictions, are shown in Fig. 4 as a function of depth for the shelf and deep

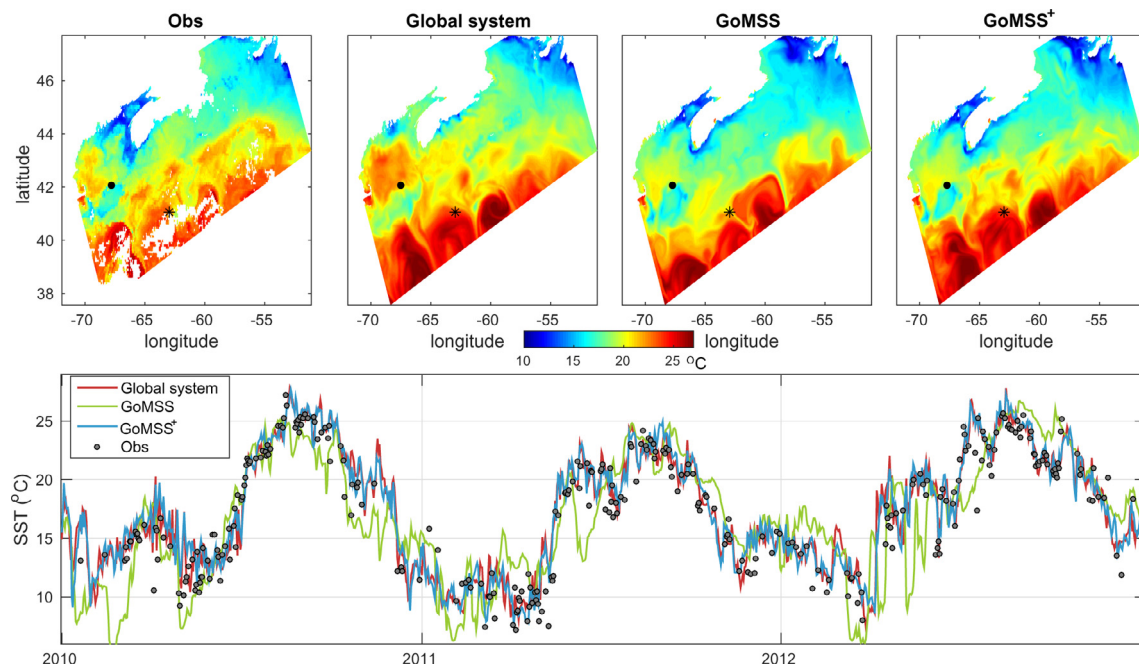


Fig. 3. Representative sea surface temperature snapshots for 22 July, 2012 based on satellite observations, the global system, GoMSS and GoMSS⁺ (top panels). The bottom panel shows the time variation of sea surface temperature for the deep water location shown by the black star on the top panels. The means and standard deviations of the difference between observed and predicted time series are listed in Table 3.

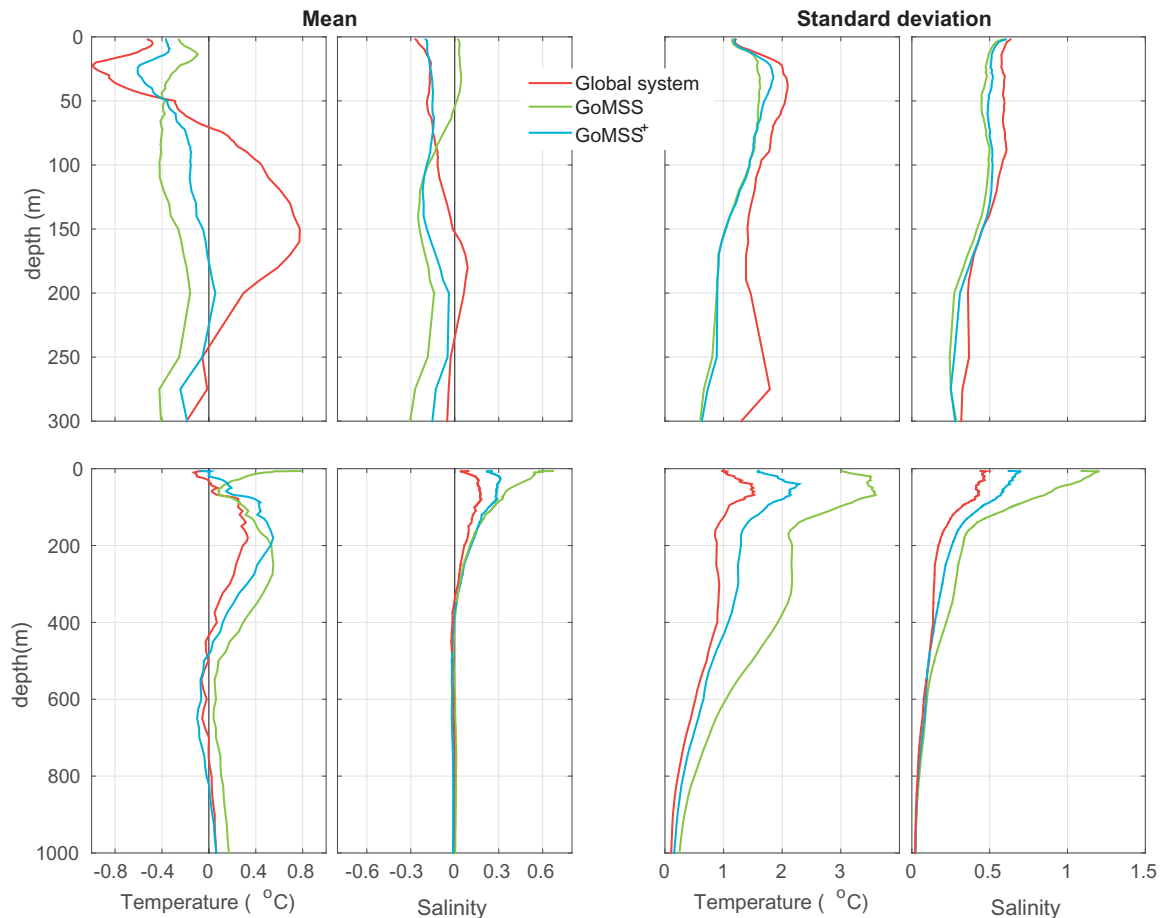


Fig. 4. Temperature and salinity mean difference (bias) and standard deviation of the difference ($\sigma_T(z)$, $\sigma_S(z)$) of observed and predicted CTD and Argo profiles as a function of depth. The locations of the profiles are shown in Fig. 2 and the y-axis of each panel shows the depth. The top panels are for the shelf ($h < 300$ m, see Fig. 2) and the bottom panels are for deep water ($h > 300$ m). Negative (positive) bias corresponds to system overestimation (underestimation). (For interpretation of the references to colour in this figure legend, the reader is referred to the web version of this article.)

water. The standard deviations of the temperature and salinity errors at depth z will henceforth be denoted by $\sigma_T(z)$ and $\sigma_S(z)$ respectively.

On the shelf, GoMSS has a smaller temperature bias than the global system over the top 200 m ($z < 200$ m). GoMSS also has smaller salinity bias (by about 0.2) for $z < 100$ m. By way of contrast, the global system has smaller salinity bias than GoMSS (by about 0.2) for $z > 100$ m. $\sigma_T(z)$ and $\sigma_S(z)$ for GoMSS are smaller than the global system values throughout the water column.

In deep water, $\sigma_T(z)$ and $\sigma_S(z)$ for the global system and GoMSS are less than 1°C and 0.1 respectively, for $z > 600$ m presumably because there is low variability of temperature and salinity at these depths. The global system has a smaller bias, $\sigma_T(z)$ and $\sigma_S(z)$ than GoMSS throughout the water column.

In summary, on the shelf GoMSS generally fits the observed temperatures and salinities better than the global system. This is not surprising because GoMSS has higher horizontal and vertical resolution and includes tidal mixing absent from the global system. Nevertheless, there are locations on the shelf (e.g., location C3 during summer) where the global system provides more accurate predictions of surface temperature. This shows that the assimilation of observations can compensate for lack of resolution and tides in the global system, particularly near the surface where most hydrographic observations are available. In deep water, the global system's predictions of temperature and salinity are in good agreement with the observations, presumably because the assimilation of satellite and in situ observations keeps the eddies and meanders

close to their true locations. By way of contrast, GoMSS's predictions of temperature and salinity have larger bias, $\sigma_T(z)$ and $\sigma_S(z)$ than the global system because GoMSS misplaces eddies and meanders (e.g., top panels of Fig. 3).

3.2. Sea level

To evaluate the sea level predicted by GoMSS we compare it to repeated profiles of sea level observed by altimeters along the six tracks shown in Fig. 1. The altimetry data are based on sea level anomalies that have been processed, validated, and distributed by CTOH/LEGOS France for coastal applications (X-Track). The data have a time spacing of 9.92 days and an along track spacing of approximately 6 km. The profiles were corrected by CTOH/LEGOS for coastal effects and aliasing by tides, storm surges and the inverse barometer effect (Roblou et al., 2011).

Hovmöller diagrams of the coastal altimeter observations along Track 4, and sea level predictions by the global system and GoMSS, are shown in Fig. 5. The high frequency variability of the model output was removed using a Butterworth filter with a cutoff frequency of 20 days (the Nyquist period of the altimeter observations). As expected, the largest variability occurs in deep water due to the effect of ocean eddies and meanders. The uniformity of the sea level signal across the shelf implies the observed coastal sea level variability is primarily due to changes in the adjacent North Atlantic. This seems to contradict previous studies where surface height has been observed to increase shoreward along the

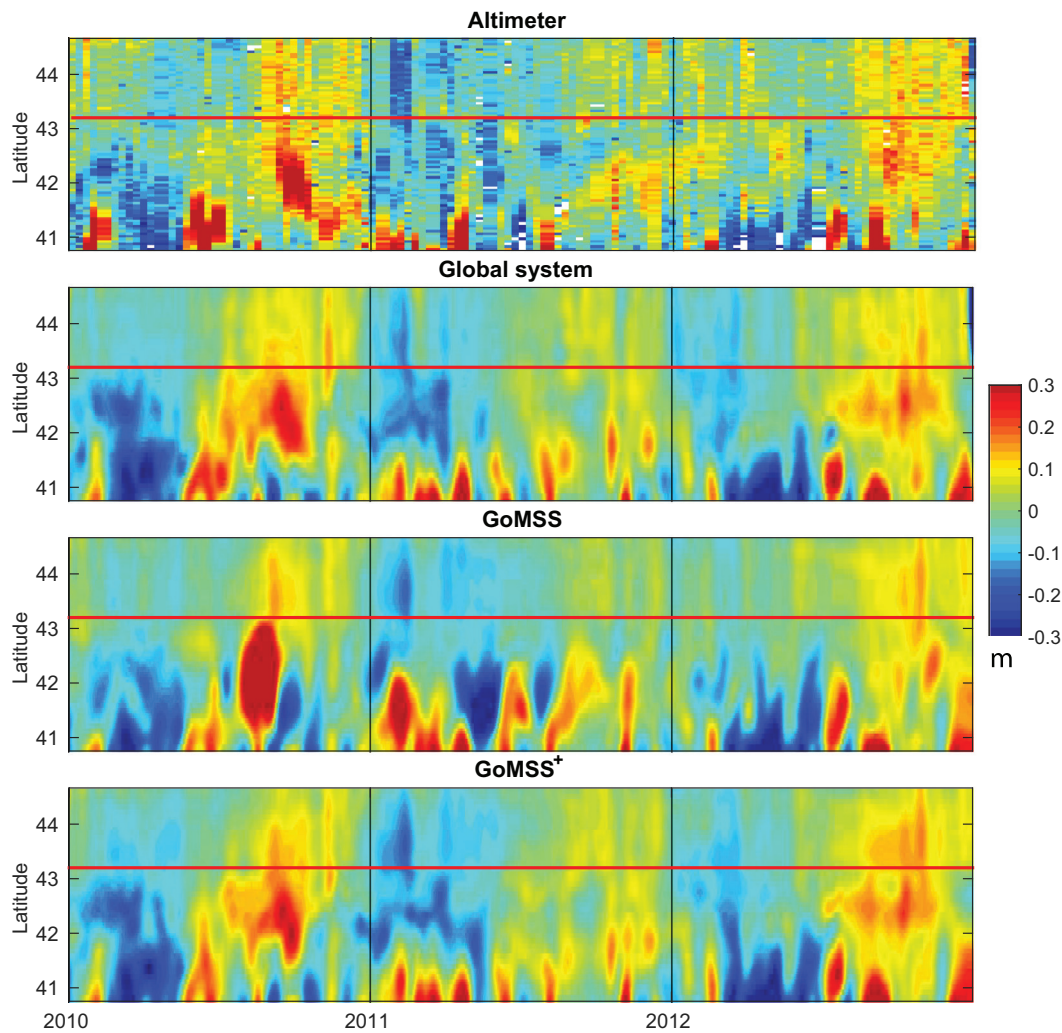


Fig. 5. Hovmöller diagrams of sea level along Track 4 (Fig. 1) based on observations from the coastal altimeter dataset (top panel), and predictions by the global system, GoMSS and GoMSS⁺. High frequency variability of all model output time series was removed using a Butterworth filter with a cutoff frequency of 20 days (the Nyquist period of the altimeter observations). The horizontal red line shows the shelf edge (near the 300 m isobath). Sea level is in meters.

Halifax Line (e.g., Loder et al., 2003). The reasons for this are not clear and further investigation (beyond the scope of the present study) is necessary to establish the dominant mechanism responsible for sea level variability across the Scotian Shelf. The largest discrepancies between the global system and GoMSS are evident in deep water. This is because the regional model and the global system place the eddies and meanders in different locations. Similar results are found for the other tracks.

Taylor diagrams (Taylor, 2001) have been used to quantify the differences between the observed and predicted sea levels along the six tracks. The results are presented separately for the shelf and deep water (Fig. 6). Note Track six runs along the Laurentian Channel and is assumed to be entirely in deep water for the purposes of this figure.

Over the shelf, along Tracks 1 and 2 (Gulf of Maine), GoMSS has slightly higher correlations with the observations and lower error standard deviations than the global system. However, GoMSS is less energetic than the observations and the global system. Over the southern part of Scotian Shelf (Tracks 3 and 4), GoMSS is in better agreement with the observations than the global system but it underestimates the observed variability by about 30%. The global system overestimates the observed variability by about 90%. Over the northern Scotian Shelf (Track 5) GoMSS and the global system have similar fits to the observations. Overall, GoMSS is in better agreement with the altimeter observations

than the global system on the shelf but is less energetic than the observations.

In deep water, along Tracks 1 to 5 the global system has significantly higher correlations with the altimeter observations and lower error standard deviations than GoMSS. For Track 6 (Laurentian Channel) the global system and GoMSS have similar statistics. Both GoMSS and the global system are less energetic than the observations for Tracks 1 to 3 and more energetic for Track 5. Overall, the global system's predictions of sea level are in better agreement with the observations than GoMSS in deep water. This is not surprising because the global system assimilates the altimeter observations.

3.3. Currents

Monthly means of observed currents archived by DFO (Ocean Data Inventory, <http://www.bio.gc.ca/science/data-donnees/base/data-donnees/odi-en.php>) are now used to evaluate the winter (January–March) and summer (July–September) seasonal mean circulation predicted by GoMSS and the global system. Only locations with multiple month records from the period 1960 to 2014 are included. Due to the limited number of observations the following discussion is supplemented by results from previous studies. Figs. 7 and 8 show the 0–100 m depth averaged seasonal circulation calculated from the observations and predicted by the global system

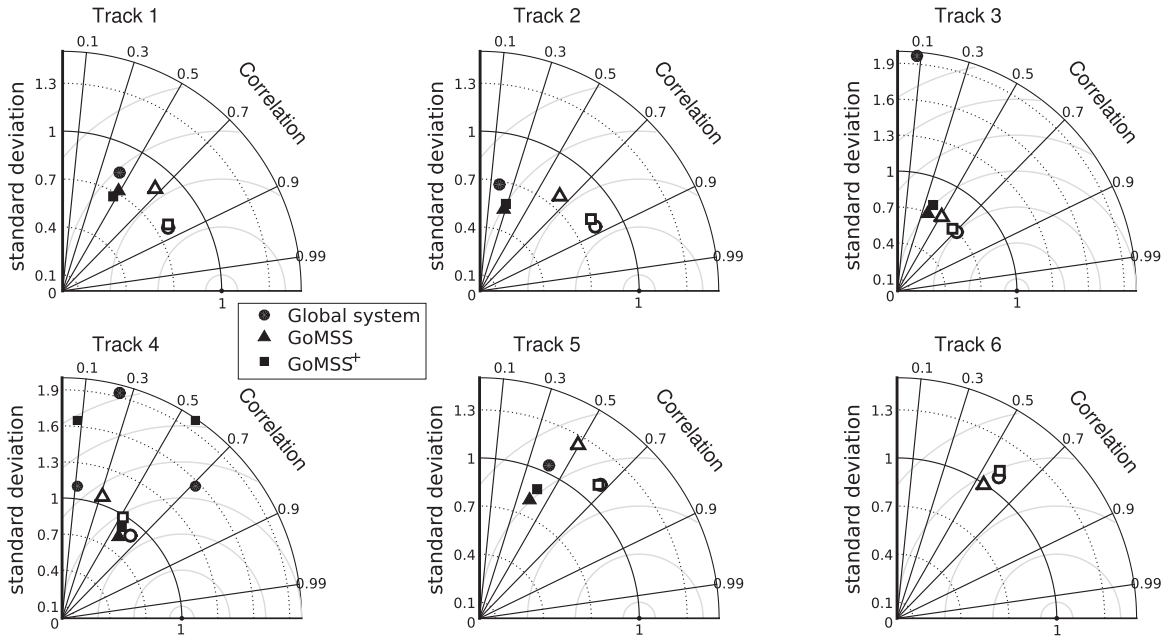


Fig. 6. Normalized Taylor diagrams comparing sea level observed by coastal altimeters with predictions by the global system, GoMSS and GoMSS+ along the six tracks shown in Fig. 1. The solid symbols are for the shelf and the open symbols for deep water.

and GoMSS. Note the observed means are based on averages of observations from different depths (depending on data availability for each location). For the scatterplots shown in the insets, and the error statistics discussed below, the predictions by the global system and GoMSS were averaged over the same depths as the observations for each location. No observations were available in deep water and so the following discussion focuses on the shelf and shelf break.

Overall, the seasonal mean currents predicted by the global system (Fig. 7) and GoMSS (Fig. 8) are in reasonable agreement with observations and previous studies (e.g., Smith, 1983; Lynch et al., 1996; Han et al., 1997; Loder et al., 1998; Hannah et al., 2001; Urrego-Blanco and Sheng, 2014). The general circulation on the shelf and along the shelf break is towards the southwest. Farther offshore, where the effect of the Gulf Stream eddies and meanders can dominate, there is an indication of flow to the northeast in summer.

GoMSS simulates well the observed clockwise circulation around Sable Island, with typical speeds of 0.08 m s^{-1} (winter) and 0.20 m s^{-1} (summer) as shown in Fig. 8. The tidally rectified current around the Sable Island, estimated by a run forced solely by the barotropic tide, with no atmospheric forcing or density variations in either space or time, reaches speeds of 0.1 m s^{-1} . This implies that tidal rectification is a major contributor to the observed clockwise circulation around Sable Island and explains why this current is not captured as accurately by the global system. Over the Gully, at the shelf break, GoMSS generates a cyclonic circulation that varies seasonally, in agreement with Han et al. (2001) and Shan et al. (2014). We speculate that the mechanism responsible for this cyclonic gyre is similar to the one discussed by Allen et al. (2001) based on conservation of potential vorticity. GoMSS and the global system simulate well the position, and summer weakening, of the Nova Scotia Current. However, during summer, the global system significantly underestimates the current speed. Comparison of Figs. 7 and 8 shows that offshore of Nova Scotia, along the shelf break, the global system predicts circulation in better agreement with the observations than GoMSS during winter.

Near Cape Sable, at the southern tip of Nova Scotia, GoMSS predicts flow from the Scotian Shelf into the Gulf of Maine dur-

ing winter, consistent with observations. GoMSS generates a clockwise circulation above Browns Bank that persists throughout the year. This flow is driven by tidal rectification and density fronts caused by intense tidal mixing on top of the Bank, consistent with previous studies (e.g., Greenberg, 1983; Hannah et al., 2001). The global system underestimates the clockwise flow on top of Browns Bank because it does not include tides. GoMSS also simulates well the clockwise circulation around Georges Bank with a peak speed in summer that exceeds 0.2 m s^{-1} along the north side of the Bank, consistent with previous studies (e.g., Loder, 1980; Butman et al., 1982; Naimie et al., 1994; Chen et al., 2001). This flow is due to tidal rectification and frontal circulation caused by intense tidal mixing on top of Georges Bank (e.g., Loder and Wright, 1985; Naimie et al., 1994; Hannah et al., 2001) and is thus missed by the global system. Along the Northeast Channel both GoMSS and the global system simulate the observed circulation that persists throughout the year: inflow towards the Gulf of Maine along the north side of the Channel and outflow along the south side. The global system underestimates the outflow along the south side of the Channel. This is because this flow is part of the clockwise circulation around Georges Bank that is related to the tidal processes discussed above. Along the coast of Maine, GoMSS predicts a cyclonic circulation that intensifies in summer in agreement with Brooks (1985) and Lynch et al. (1996). The global system does not capture this flow during summer.

To assess the predictions of observed seasonal mean currents by the global system and GoMSS, the following regression model was used:

$$\mathbf{u}_{obs} = \boldsymbol{\beta}_0 + \mathbf{u}_{mod}\boldsymbol{\beta}_1 + \epsilon \quad (6)$$

where \mathbf{u}_{obs} and \mathbf{u}_{mod} denote the co-located observed and modelled seasonal mean currents respectively, and ϵ denotes the error. All variables and regression coefficients are assumed to be complex. The intercept $\boldsymbol{\beta}_0$ corresponds to a large scale flow not captured by the ocean model. $\boldsymbol{\beta}_1$ scales and rotates the model currents to best fit the observations. $|\boldsymbol{\beta}_1|$ smaller (greater) than one corresponds to model overestimation (underestimation) of the observed current speed.

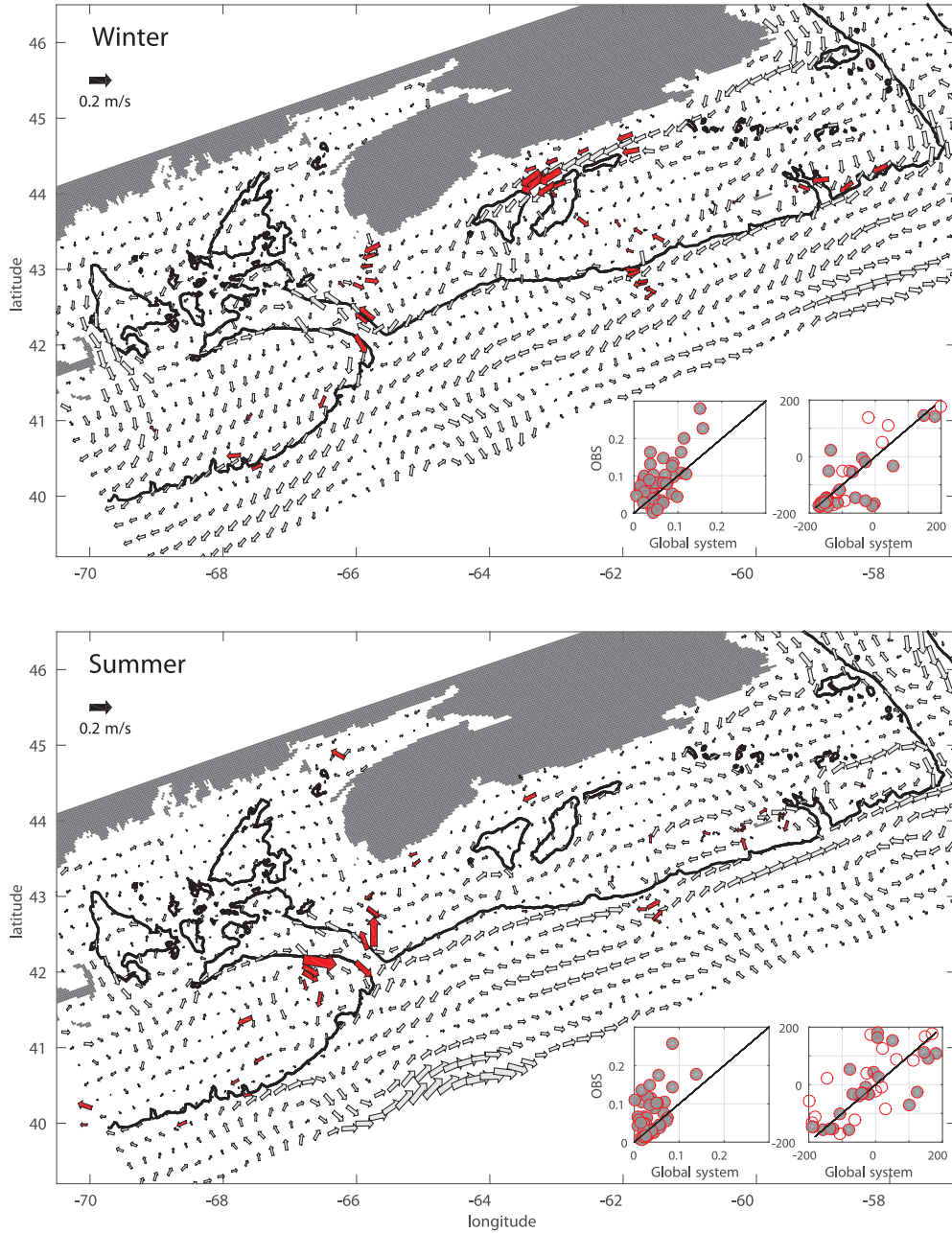


Fig. 7. Comparison of observed (red arrows) and predicted (black arrows) currents averaged over the top 100 m. The predictions are from the global system for 2010–2012 and are shown every 3rd grid point. The black lines show the 200 m isobath. The insets are scatterplots of observed and predicted speed (m s^{-1}) and direction (degrees, clockwise from eastward). The open circles corresponds to directions of currents with speed less than 0.05 m s^{-1} . The top panel is for winter (January–March) and the bottom panel is for summer (July–September). (For interpretation of the references to colour in this figure legend, the reader is referred to the web version of this article.)

The estimates of β_0 and β_1 were obtained using complex least squares and are denoted by $\hat{\beta}_0$ and $\hat{\beta}_1$. The predicted mean flow is then given by $\hat{\mathbf{u}} = \hat{\beta}_0 + \mathbf{u}_{\text{mod}} \hat{\beta}_1$ and we use the following statistic to quantify model fit:

$$R^2 = \frac{\sum_{i=1}^{N_{\text{obs}}} |\hat{\mathbf{u}}_i|^2}{\sum_{i=1}^{N_{\text{obs}}} |\mathbf{u}_{\text{obs}_i}|^2} \quad (7)$$

where N_{obs} is the number of observed seasonal means. Note that R^2 is constrained to be between 0 and 1. Further details about the above regression model and R^2 are given by Katavouta et al. (2015).

$\hat{\beta}_0$, $\hat{\beta}_1$ and R^2 for the global system and GoMSS are listed in Table 4. For both systems $|\hat{\beta}_0|$ is small (less than 2.8 cm s^{-1}). During winter, the global system and GoMSS have similar skill

($R^2 = 0.63$ and 0.62 , respectively). The global system underestimates the current speed ($|\hat{\beta}_1| > 1$) while GoMSS overestimates it. However, they both have small rotation error indicating they simulate well the direction of the mean circulation during winter. During summer the skill of GoMSS and the global system both drop and their rotation error increases. However, GoMSS has higher skill than the global system during this season.

In deep water the global system and GoMSS predict very different circulation patterns. The lack of current observations for the deep water means we cannot say which pattern is the most realistic based on this data source. However, comparisons with surface temperature and sea level (Figs. 3 and 5) discussed above strongly suggest the global system correctly places most of the large scale patterns in deep water. It is also clear that GoMSS

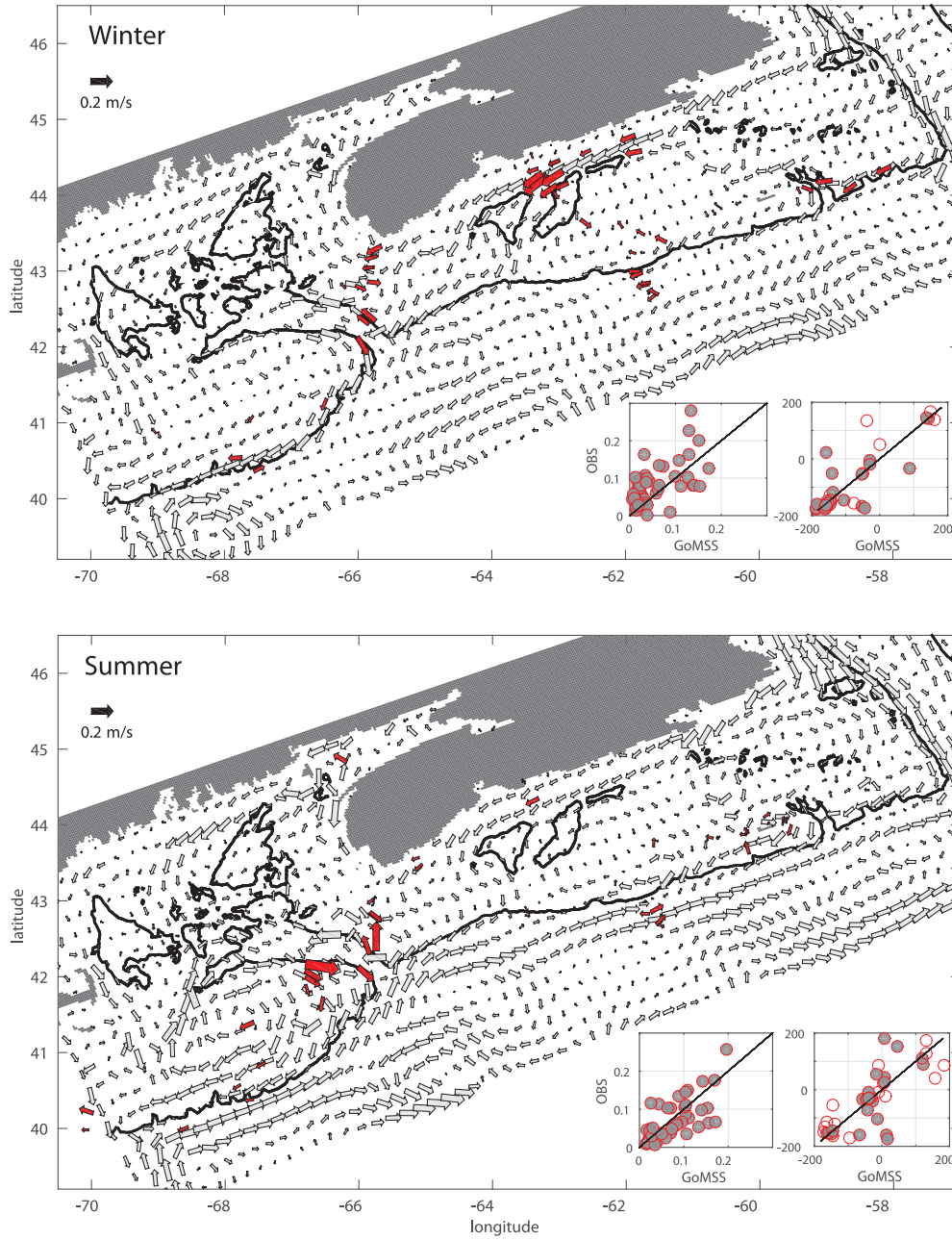


Fig. 8. Comparison of observed (red arrows) and predicted (black arrows) currents averaged over the top 100 m. The predictions are from GoMSS for 2010–2012 and are shown every 9th grid point. Otherwise same format as Fig. 7. (For interpretation of the references to colour in this figure legend, the reader is referred to the web version of this article.)

Table 4

Prediction of observed seasonal mean currents by the global system, GoMSS and GoMSS+ in both winter and summer. The complex regression coefficients $\hat{\beta}_0$ and $\hat{\beta}_1$ (see (6)) are given in polar form. $|\hat{\beta}_0|$ is in cm s^{-1} and $|\hat{\beta}_1|$ has no units. The angles of $\hat{\beta}_0$ and $\hat{\beta}_1$ are both in degrees measured counter clockwise from east. R^2 has no units and lies between 0 and 1.

	Global system		GoMSS		GoMSS+	
	Winter	Summer	Winter	Summer	Winter	Summer
$\hat{\beta}_0$	(1.2, -162)	(2.8, -160)	(1.8, -171)	(1.3, 156)	(2.1, -168)	(1.5, 174)
$\hat{\beta}_1$	(1.16, -0.6)	(1.22, 6.8)	(0.82, 2.4)	(0.81, 7.0)	(0.80, 2.5)	(0.93, 8.1)
R^2	0.63	0.31	0.62	0.43	0.61	0.48

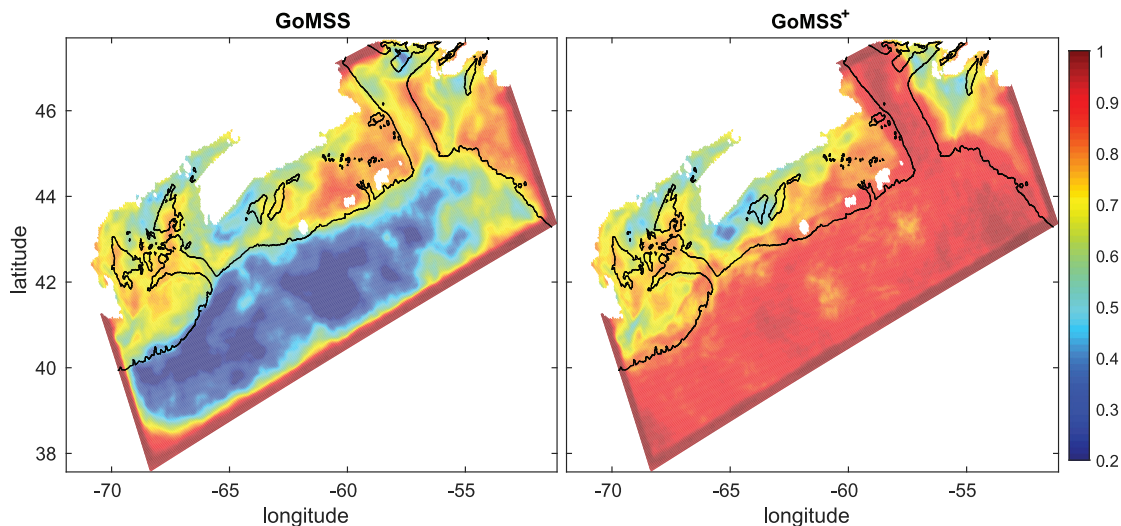


Fig. 9. Correlation of temperature predicted by the global system with temperature predicted by (left panel) GoMSS and (right panel) GoMSS⁺. The correlation is based on daily temperatures from the global and regional systems for the same time (no time lag) and the same point (co-located). The black lines show the 200 m isobath. The temperatures were averaged over the top 20 m, and the annual and the semiannual cycles were removed, before calculating the correlation. Based on data for the period 2010–2012.

generates some unrealistic circulation features near its lateral open boundaries, e.g., the persistent clockwise circulation near the west open boundary shown in Fig. 8. We return to this point in the following subsection.

3.4. Internal Variability and Recirculation near Lateral Open Boundaries

As discussed in the Introduction, all nonlinear regional models are affected by internally generated variability to some degree. To illustrate the effect of such variability, the left panel of Fig. 9 is a map of the correlation between co-located values of daily temperature, averaged over the top 20 m, from GoMSS and the global system. In other words, this figure shows the strength of the linear relationship between co-located, and contemporaneous, near surface temperatures predicted by the global system and GoMSS. A value close to zero shows that the global system and GoMSS predict very different temperatures at this grid point, i.e., their variability has decoupled. A value close to one shows that both the global system and GoMSS predict similar temperatures at this location. Note the annual and semi-annual cycles were removed before calculating the correlations and so the seasonal cycle does not affect the correlations.

On the shelf, surface temperature is driven by atmospheric forcing, mixing and advection. Both the global system and GoMSS have similar atmospheric forcing. GoMSS represents better the mixing and circulation on the shelf because of its tides and higher resolution, however, the global system compensates for the absence of tides and lower resolution by assimilating observations (e.g., surface temperature from satellites). Thus, it is not surprising that Fig. 9 indicates the correlations between the co-located temperatures predicted by the global system and GoMSS generally exceed 0.5 on the shelf.

In the sponge layer adjacent to the lateral open boundaries, the temperatures predicted by the global system and GoMSS are strongly correlated as expected (Fig. 9). However, the correlation drops rapidly moving from the sponge layer to the model interior. This drop in correlation is the result of internal variability: GoMSS and the global system both generate eddies, meanders and fronts, but they place them at different locations. This can be seen more clearly in Fig. 10 which shows Hovmöller diagrams of the

vertical component of relative vorticity, normalized by the planetary vorticity, along the blue line in deep water defined in Fig. 1. Fig. 10 shows that GoMSS predicts more small scale vorticity than the global system which is not surprising given its higher resolution. It can also be seen however, that there are large differences in the locations of many of the major vorticity features predicted by GoMSS and the global system. Thus, further control beyond one-way nesting is required to ensure GoMSS is consistent with the fields introduced along its lateral open boundaries.

Note that although a radiation algorithm, with different relaxation coefficients for inflow and outflow, was used along GoMSS lateral open boundaries in an attempt to allow perturbations to leave the model domain, perturbations remained trapped within the domain leading to unrealistic recirculation near the lateral open boundaries. The recirculation occurs in areas where GoMSS has large outflow in contrast to the global system (the source of the lateral open boundary condition) which has weaker outflow, or possibly inflow. To illustrate, Fig. 8 shows an unrealistic anticyclonic eddy located adjacent to the west open boundary.

Several sensitivity experiments, based on varying the outflow relaxation strength, were performed in an attempt to reduce the unrealistic circulation features near the lateral open boundaries of GoMSS. Very strong relaxation led to more unrealistic recirculation near the boundaries, however, it kept the model outflow locations consistent with the global system. Very weak relaxation limited the recirculation but caused areas of outflow that were inconsistent with the global system. Even allowing for different relaxation times along the four lateral open boundaries could not remove these unrealistic circulation patterns.

In summary, on the shelf GoMSS predicts temperature, salinity, sea level and seasonal mean circulation more accurately than the global system. In deep water, GoMSS's predictions differ greatly from the global system and the observations. This is because GoMSS is affected by unrealistic internal variability and recirculation features near its lateral open boundaries. Note that previous studies using one-way nested regional models have identified similar problems related to the open boundary across the New England Shelf (e.g., Naimie et al., 1994; Hannah et al., 2001; Brickman and Drozdowski, 2012). In the next section we investigate if spectral nudging can suppress these unrealistic features.

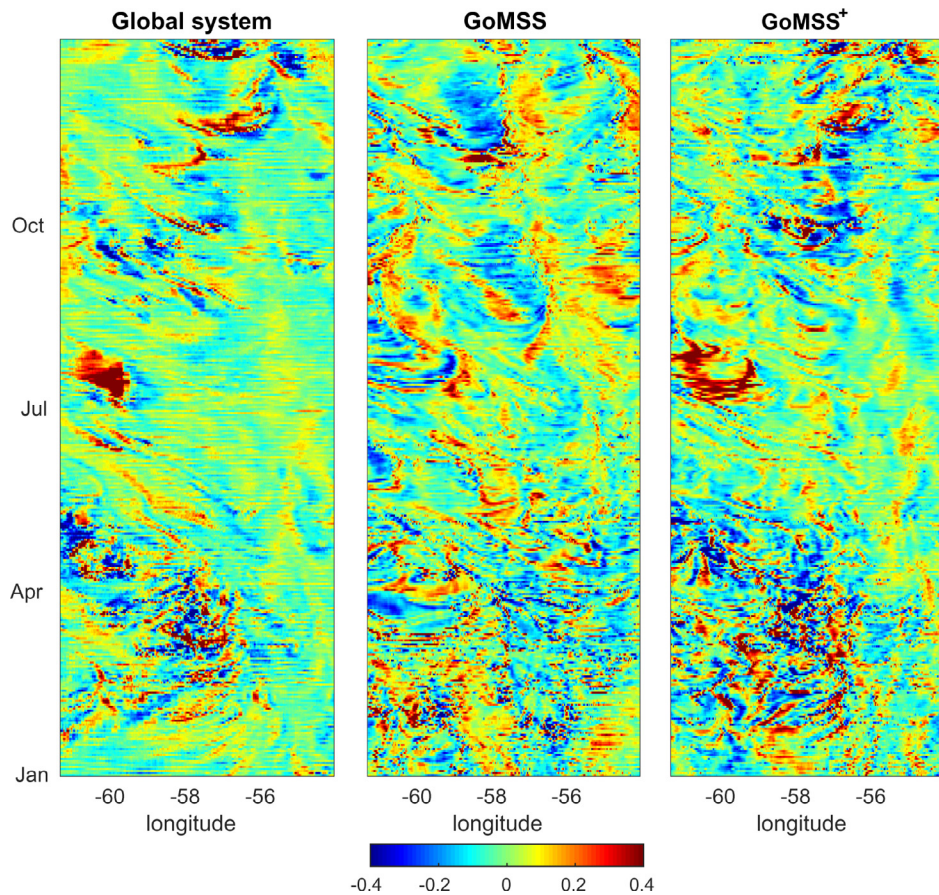


Fig. 10. Hovmöller diagrams of relative vorticity, normalized by planetary vorticity, defined along the blue line in deep water shown in Fig. 1. The length of the line is about 650 km. Vorticity was calculated from the daily fields of surface velocity predicted by the global system, GoMSS and GoMSS⁺ for 2012.

4. Impact of spectral nudging

We now examine if spectral nudging of the large scales can improve the realism of GoMSS. GoMSS⁺ is evaluated by comparing its predictions with those of the global system and GoMSS, and also the observations. To simplify the discussion, the deep water and shelf are discussed separately.

4.1. Deep water

A typical snapshot of surface temperature predicted by GoMSS⁺ is shown in the rightmost top panel of Fig. 3. GoMSS⁺ places the front between the warm off-shelf water and cold on-shelf water, and the associated eddies, at locations consistent with the observations and the global system, e.g., spectral nudging has removed an unrealistic meander in the vicinity of 60°W and 41°N. Furthermore, GoMSS⁺ predicts variations in surface temperature that are in closer agreement with the observations than GoMSS and have slightly smaller error standard deviations than the global system (bottom panel of Fig. 3, Table 3). These results indicate that GoMSS⁺ has successfully ingested the large scales of the global system and that spectral nudging has reduced the unrealistic internal variability. This can also be seen in Fig. 9 which shows that spectral nudging eliminates the decoupling of surface temperatures predicted by GoMSS and the global system in deep water.

Below the surface, and beyond the shelf break, GoMSS⁺ predicts vertical profiles of temperature and salinity that are in better agreement with the observations than GoMSS (see Appendix B). Quantitative comparison with the hydrographic observations (Fig. 4) reveals that spectral nudging has reduced both

the temperature and salinity bias, $\sigma_T(z)$ and $\sigma_S(z)$ of GoMSS throughout the water column in deep water. The global system still has smaller bias, $\sigma_T(z)$ and $\sigma_S(z)$ than GoMSS⁺ because it assimilates the observed vertical profiles.

It is not surprising that spectral nudging significantly changes GoMSS temperature and salinity in the deep water because it assimilates information on their large scales. However, spectral nudging also modifies variables that are not directly nudged. To demonstrate, sea level predicted by GoMSS⁺ is in better agreement with the observations than GoMSS along Track 4 (Fig. 5). It can be seen, for example, that spectral nudging has eliminated an unrealistic sea level anomaly occurring between 41°N and 43°N in the late summer of 2010. The Taylor diagrams (Fig. 6) confirm that GoMSS⁺ is in better agreement with the altimeter data along Tracks 1 to 5 in the deep water. Along Track 6 all the three systems have similar sea level statistics. As expected, the sea level predictions by the global system are in slightly better agreement with the observations than GoMSS⁺ in deep water because the global system assimilates these observations.

GoMSS⁺ predictions of the winter and summer mean circulation are shown in Fig. 11. Comparisons with GoMSS (Fig. 8) and the global system (Fig. 7) show that in deep water GoMSS⁺ is more consistent with the global system than GoMSS in both winter and summer. GoMSS⁺ does not generate unrealistic recirculation along the west and south open boundaries. This is encouraging because it shows that spectral nudging has eliminated the trapped eddies associated with ill-posed open boundary conditions.

Overall, spectral nudging places the large scale features at locations consistent with the global system in the deep water. Fig. 10 shows that the global system and GoMSS⁺ place most of

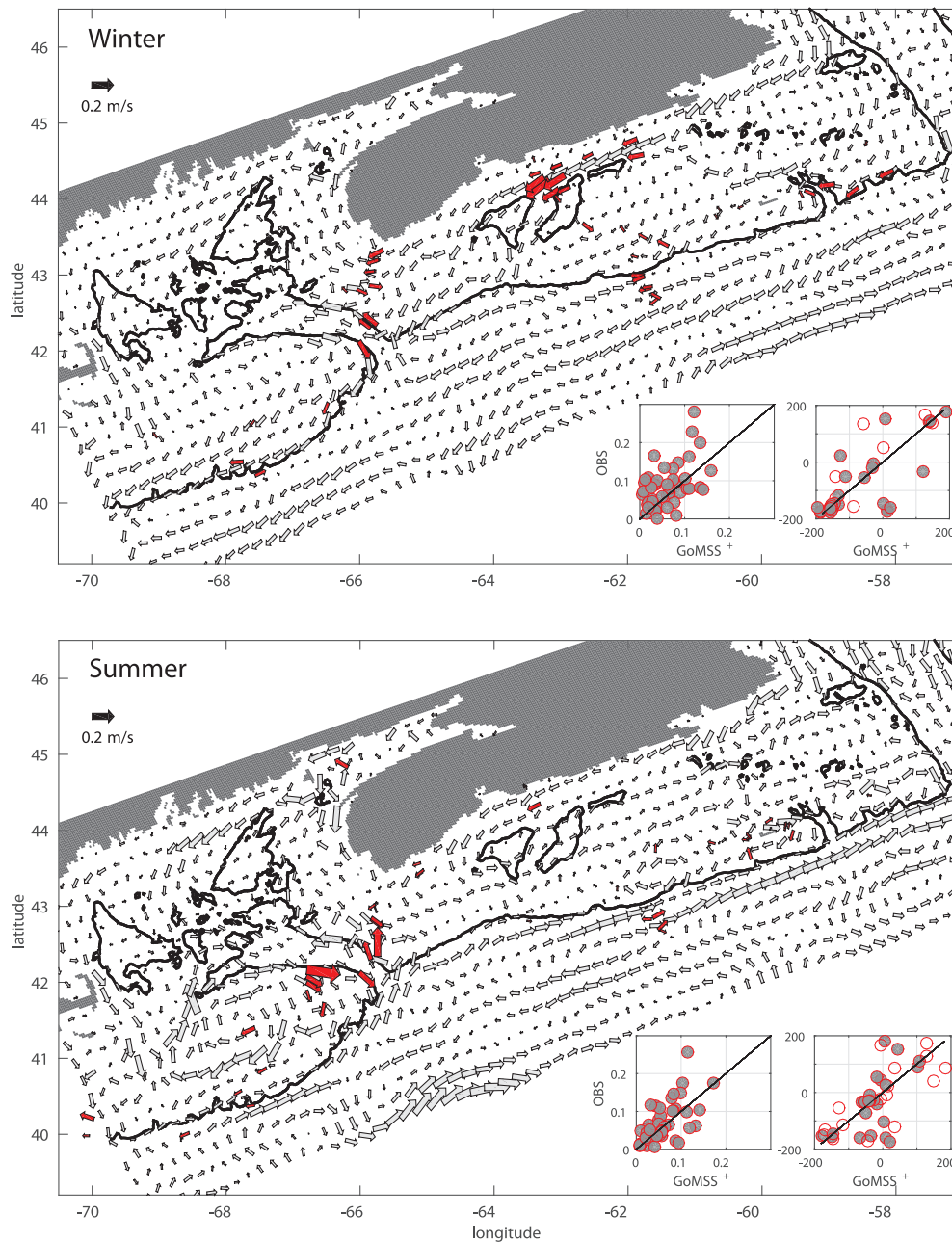


Fig. 11. Comparison of observed (red arrows) and predicted (black arrows) currents averaged over the top 100 m. The predictions are from GoMSS⁺ for 2010–2012 and are shown every 9th grid point. Otherwise same format as Fig. 7. (For interpretation of the references to colour in this figure legend, the reader is referred to the web version of this article.)

the major features in the relative vorticity at approximately the same locations. However, GoMSS⁺ generates more small scale vorticity than the global system which suggests that spectral nudging has not suppressed the small scale variability in deep water. We return to this point in Section 5.

4.2. Shelf

GoMSS⁺ and GoMSS predict similar temperatures and salinities on the shelf and they are generally in better agreement with the observations than the global system (Table 3, Figs. 3 and 4 and Appendix B). This is not surprising because there is only weak nudging in the vicinity of the shelf break and no nudging on the shelf. Within 80 m of the surface GoMSS has smaller temperature and salinity bias than GoMSS⁺ (Fig. 4). By way of contrast, GoMSS⁺

has smaller temperature and salinity bias below 80 m than GoMSS. The major contribution to this change in bias comes from areas close to the shelf break where weak nudging is applied.

GoMSS⁺ predicts sea levels that are more consistent with the observations than the global system along Track 4 (Fig. 5). The Taylor diagrams (Fig. 6) confirm that, overall, GoMSS⁺ predicts sea levels that are in better agreement with the observations than the global system, similar to GoMSS, on the shelf. GoMSS⁺ sea levels are slightly more energetic than GoMSS along Tracks 2, 3, 4 and 5, consistent with observations.

GoMSS⁺ and GoMSS predict similar seasonal circulations (compare Figs. 11 and 8) on the shelf. GoMSS⁺ simulates well the Nova Scotia Current, the observed clockwise circulation around Sable Island (similar to GoMSS) and its summer intensification, and the cyclonic circulation and its seasonal variation over the Gully.

Similar to GoMSS, GoMSS⁺ generates the flow from the Scotian Shelf into the Gulf of Maine near Cape Sable and the overall cyclonic circulation in the Gulf of Maine and its intensification during summer. Additionally, GoMSS⁺ generates the clockwise circulations over Georges and Browns Banks (associated with tidal rectification and frontal circulation) that persist throughout the year. Nevertheless, GoMSS and GoMSS⁺ have some differences. For example, during summer GoMSS⁺ generates i) a more limited clockwise circulation on top of Emerald Bank that does not extend north of the Bank and into Emerald Basin as in GoMSS, ii) a stronger northward flow north of Emerald Bank, in agreement with the observations and iii) a weaker southward flow along the south edge of Georges Bank. Table 4 shows that during winter GoMSS⁺ has similar skill ($R^2 = 0.61$) to GoMSS and the global system but higher skill in summer.

In summary, in deep water GoMSS⁺ predictions are in better agreement with the observations than GoMSS. Spectral nudging places the front between the slope and the shelf water, and the associated eddies and meanders, in positions that are more consistent with the global system and the observations. On the shelf the predictions by GoMSS⁺ and GoMSS are similar (except close to the shelf break where some weak nudging occurs) and better than the global system. Overall, GoMSS⁺ leads to realistic predictions both on the shelf and in the deep water. Note that the internal tides, and their dependence on the local bathymetry and seasonal stratification, is the same in GoMSS and GoMSS⁺ (not shown).

5. Impact of downscaling on wavenumber spectra

In the three systems the energy supply, removal and distribution are influenced by the surface and bottom boundary conditions. However, the energy balances of the three systems are also influenced by i) the assimilation of observations in the global system, ii) the lateral open boundary conditions in GoMSS and GoMSS⁺, and iii) spectral nudging in GoMSS⁺ which directly affects the energy of the large scales, and indirectly affects the small scales through the model's nonlinear dynamics.

In deep water the global system assimilates all of the readily available observations; thus, they cannot be used to provide a fair assessment of the global system and GoMSS⁺. To evaluate the performance of GoMSS⁺ on length scales that are not directly affected by spectral nudging, and investigate the distribution and transfer of energy in the three systems, we now examine the wavenumber dependence of their sea level variance, kinetic energy and enstrophy.

The wavenumber spectra for sea level, eddy velocity (leading to eddy kinetic energy) and eddy vorticity (leading to eddy enstrophy per unit area) are denoted by $S(k)$, $\mathcal{E}(k)$ and $\mathcal{Z}(k)$ respectively where k is the wavenumber. Spectra for a given geographic line are estimated by i) removing the spatial and time average of each variable (resulting in an “eddy” perturbation), ii) applying discrete Fourier transforms along the line for each time, iii) squaring the absolute value of each Fourier component, and iv) averaging through time. A factor of 1/2 is applied to $\mathcal{E}(k)$ and $\mathcal{Z}(k)$ for consistency with the usual definitions of energy and enstrophy. The analysis below focuses on surface variability.

5.1. Deep water

Wavenumber spectra in variance preserving form were estimated at the surface along the blue line in deep water shown in Fig. 1. This line was chosen because the variations of sea level, surface velocity and relative vorticity are approximately stationary in both space and time along the line. Spectra along several other lines in deep water (with different length and locations), outside the sponge layer, gave similar results.

The top right panel of Fig. 12 shows that, overall, GoMSS has higher sea level variance than the global system and GoMSS⁺ for all length scales. This is not surprising because GoMSS generates unrealistic internal variability (e.g., Figs. 5 and 9). Particularly, the trapped perturbations, associated with the lateral open boundary conditions, are probably responsible for GoMSS high sea level variance. GoMSS⁺ has a sea level spectrum that is similar to the global system due to the nudging of temperature and salinity for wavelengths larger than the critical cutoff wavelength ($\lambda > 90$ km). There is not much sea level variability for wavelengths $\lambda < 100$ km. Thus it is difficult to use sea level to determine which system generates more small scale variability. As an aside we note that a log-log plot of the sea level spectra (not shown) reveals that, for $\lambda < 250$ km, sea level approximately follows a $k^{-11/3}$ spectrum for all the three systems, consistent with altimeter observations (LeTraon et al., 2008).

A Log-log plot of the kinetic energy spectra (not shown) reveals that all three systems approximately follow a $k^{-5/3}$ spectrum for $80 < \lambda < 250$ km, and a k^{-3} spectrum for $15 < \lambda < 80$ km. Thus, according to geostrophic turbulence theory (Vallis, 2006; Ferrari and Wunsch, 2009), the inverse energy cascade (energy transfer to larger scales) occurs at $\lambda > 80$ km which is about three times the first Rossby radius of deformation for the deep water region. The reason for this is not clear but Vallis (2006) notes that the wavelength of maximum instability can be expected to exceed the first deformation radius, as in the Eady problem. For $\lambda > 250$ km the inverse cascade is halted probably due to the influence of the β -effect and bottom friction (Rhines, 1975). For $\lambda < 15$ km, where ageostrophic dynamics becomes important, the energy spectra have a slope close to $-5/3$ associated with a forward cascade, consistent with previous studies (e.g., Capet et al., 2008).

In deep water, the kinetic energy spectra (middle right panel of Fig. 12) show that, overall, GoMSS is more energetic than the global system. This is expected for the small scales because GoMSS has higher resolution than the global system. However, for the large wavelengths this is probably associated with the unrealistic recirculation occurring due to problems with the lateral open boundary conditions that can lead to unrealistic high variability in deep water. For $\lambda > 160$ km GoMSS⁺ is somewhat less energetic than the global system. This is because spectral nudging does not directly influence the velocity and thus the associated kinetic energy. However, GoMSS⁺ has more energy than the global system, and GoMSS, for $10 < \lambda < 100$ km in deep water. This confirms that spectral nudging does not suppress the variability below the critical cutoff wavelength ($\lambda < 90$ km) and leads us to speculate that it acts as a source of potential energy that “feeds” the kinetic energy (through baroclinic instability) and thus the formation of eddies with wavelengths between 10 km and 100 km.

The enstrophy spectra in deep water (bottom right panel of Fig. 12) for the global system and GoMSS are similar for $\lambda > 30$ km. All systems have an enstrophy spectral peak at $\lambda \approx 50$ km in the variance preserving form used in Fig. 12. However, GoMSS⁺ generally has more enstrophy than both the global system and GoMSS, and a sharper peak. This implies that spectral nudging acts as an additional enstrophy source in the deep water. The reason is that in deep water, the eddies are primarily generated by baroclinic instability (i.e., transfer of potential energy to kinetic energy), in contrast to the shelf where other mechanisms dominate the generation of small scale motions (e.g., atmospheric forcing over variable bathymetry, tidal mixing and rectification).

5.2. Shelf

We now discuss the wave-number spectra estimated at the surface along the shelf line shown in Fig. 1. Spectra along other shelf lines gave similar results. The top left panel of Fig. 12 shows the

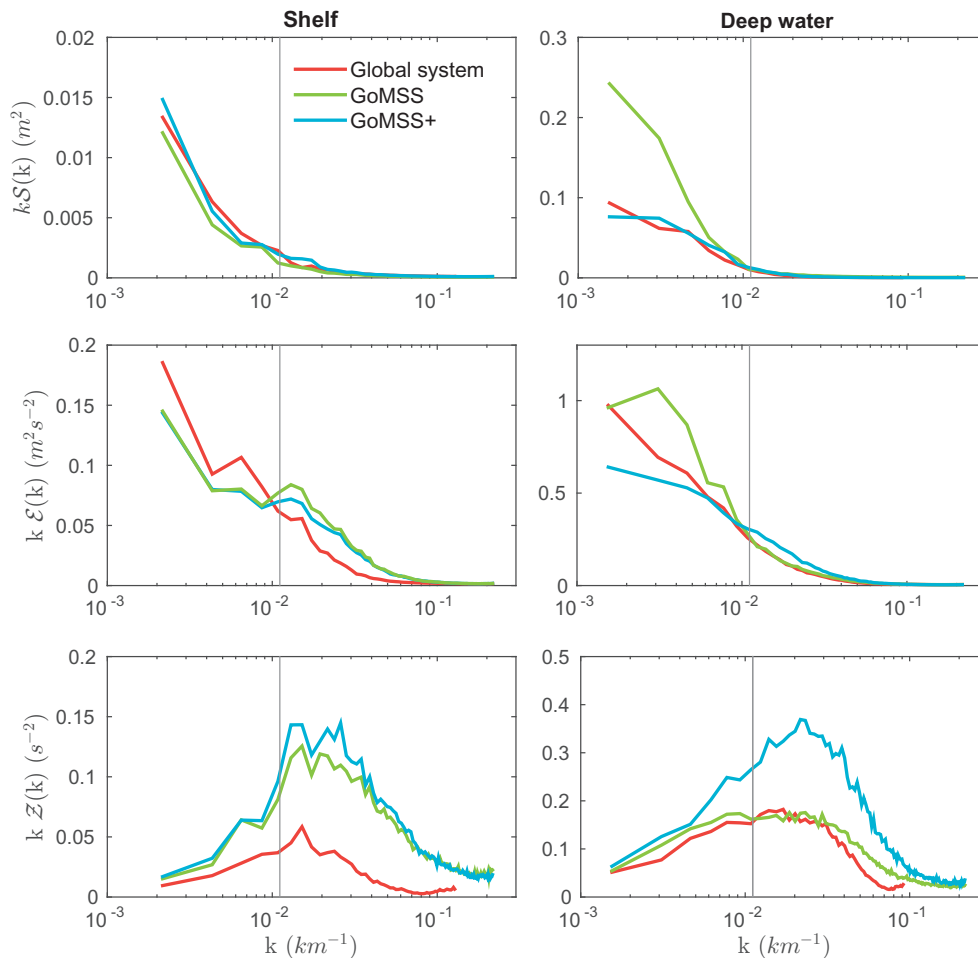


Fig. 12. Wave-number decomposition of sea level variance (top panels), turbulent kinetic energy (middle panels) and turbulent enstrophy (bottom panels) shown in variance preserving form. The spectra were calculated from surface predictions made along the two blue lines (Fig. 1) on the shelf (left panels) and in deep water (right panels). The grey vertical lines show the spectral nudging cutoff wavenumber, $1/\lambda_c$. Wavenumber, shown on the x-axis, is in cycles per km. (For interpretation of the references to colour in this figure legend, the reader is referred to the web version of this article.)

sea level spectra for the three systems are similar and there is almost no sea level variance for wavelengths below 100 km. The kinetic energy and enstrophy spectra for GoMSS and GoMSS+ are almost identical (middle and bottom left panels of Fig. 12). This is to be expected because the dynamical processes dominating the generation of variability (e.g., advection, atmospheric forcing, tidal rectification and mixing) are the same in GoMSS and GoMSS+. The global system has weaker energy and enstrophy than GoMSS and GoMSS+ for $\lambda < 100$ km. This confirms that the regional model generates more small scale variability than the global system because it has higher resolution and includes tides.

6. Summary and discussion

As a part of a broader study of ocean downscaling, we developed a high resolution regional model of the Gulf of Maine, Scotian Shelf and adjacent North Atlantic in order to resolve processes that are important on the shelf and yet absent from the present generation of operational global systems (e.g., tides and their effect on circulation and stratification). In a previous study, (Katavouta et al., 2015) showed that this regional model, in a simple one-way nesting configuration, provides realistic predictions of the tides and the dynamical interaction of variability on the seasonal and tidal time scales. In the present study, we have further investigated the regional model's realism, based on comparisons with in-situ and

satellite observations, and identified strengths and weaknesses of the regional model in its one-way nested configuration.

In the Gulf of Maine and on the Scotian Shelf the regional model improves the realism of the global system. This shows that the explicit representation of finer scales and tides in the regional model outperforms the assimilation of observations by the global system.

In deep water, the assimilation of observations ensures that the global system place features such as eddies and meanders at their correct locations. The regional model decouples from the global system just beyond the sponge layer along the lateral open boundaries. This is the result of the regional model's generation of unrealistic internal variability in deep water. Furthermore, the regional model generates unrealistic recirculation features close to the lateral open boundaries that we could not suppress by "tuning" of the open boundary conditions.

Spectral nudging of the regional model eliminates the decoupling of the regional and global models and suppresses the unrealistic recirculations near the lateral open boundaries. Spectral nudging also places the large scale features at the correct locations in deep water. Spectral nudging combines the strengths of the regional model (i.e., explicit representation of small scale dynamics and tides) and the global system (i.e., placing the eddies and meanders at the observed locations) and so generates realistic fields both on and off the shelf.

Energy and enstrophy spectra show that even though spectral nudging only updates length scales exceeding 90 km, it also indirectly modifies the kinetic energy and enstrophy of the smaller scales in deep water through the nonlinearity of the governing equations. More specifically, spectral nudging supplies kinetic energy to wavelengths between 10 km and 100 km and enstrophy to all wavelengths.

Turning to future work, detailed energy and enstrophy budgets are required to better understand how spectral nudging affects the variability below the wavenumber cutoff of $\lambda_c = 90$ km. From a practical perspective, more test cases and sensitivity experiments are required to provide guidelines for the specification of the spectral nudging parameters, including their spatial and possibly seasonal variation.

As a final remark, we note that the method discussed in this study should not be seen as a substitute for the assimilation of observations into the regional model if they are available. Katavouta and Thompson (2013) noted that spectral nudging combined with assimilation of local observations will apply corrections to all length scales and may account for imperfections in the global system fields that are introduced to the regional model through the open boundary conditions and the spectral nudging of the large scales. This is significant because although the global model assimilates observations, these observations are not used to their full potential (e.g., observations are thinned prior to assimilation) and thus only correct the length scales resolved by the global model. Although the present study focuses on spectral nudging, it is part of a broader effort to develop a relocatable ocean forecast system that can be used to help guide response to marine emergencies.

Thus, we are currently working on implementing data assimilation into a relocatable version of GoMSS+ designed to extract as much information as possible from the global model and local observations.

Acknowledgments

The authors thank Dr. Youyu Lu, Dr. John W. Loder and two anonymous reviewers for many constructive and insightful comments. This work was supported by the Ocean Tracking Network (OTN) Canada through a strategic network Grant (NETGP 375118-08) from the Natural Sciences and Engineering Research Council of Canada (NSERC), and the Marine Environmental Observation Prediction and Response Network (MEOPAR), one of Canada's Networks of Centers of Excellence.

Appendix A. Frequency dependent and spectral nudging

Thompson et al. (2006) and Wright et al. (2006) developed and applied a method for suppressing bias and drift of ocean models. Initially this method was developed to nudge a model towards an observed climatology in selected frequency bands and the authors initially referred to their approach as frequency dependent nudging. They subsequently changed the name to spectral nudging after they started spatially smoothing the frequency dependent nudges (i.e., they nudged in prescribed frequency and wave-number bands). The use of the same name (spectral nudging) for two approaches (nudging in frequency and/or wave-number bands) may cause confusion. The form of spectral nudging used

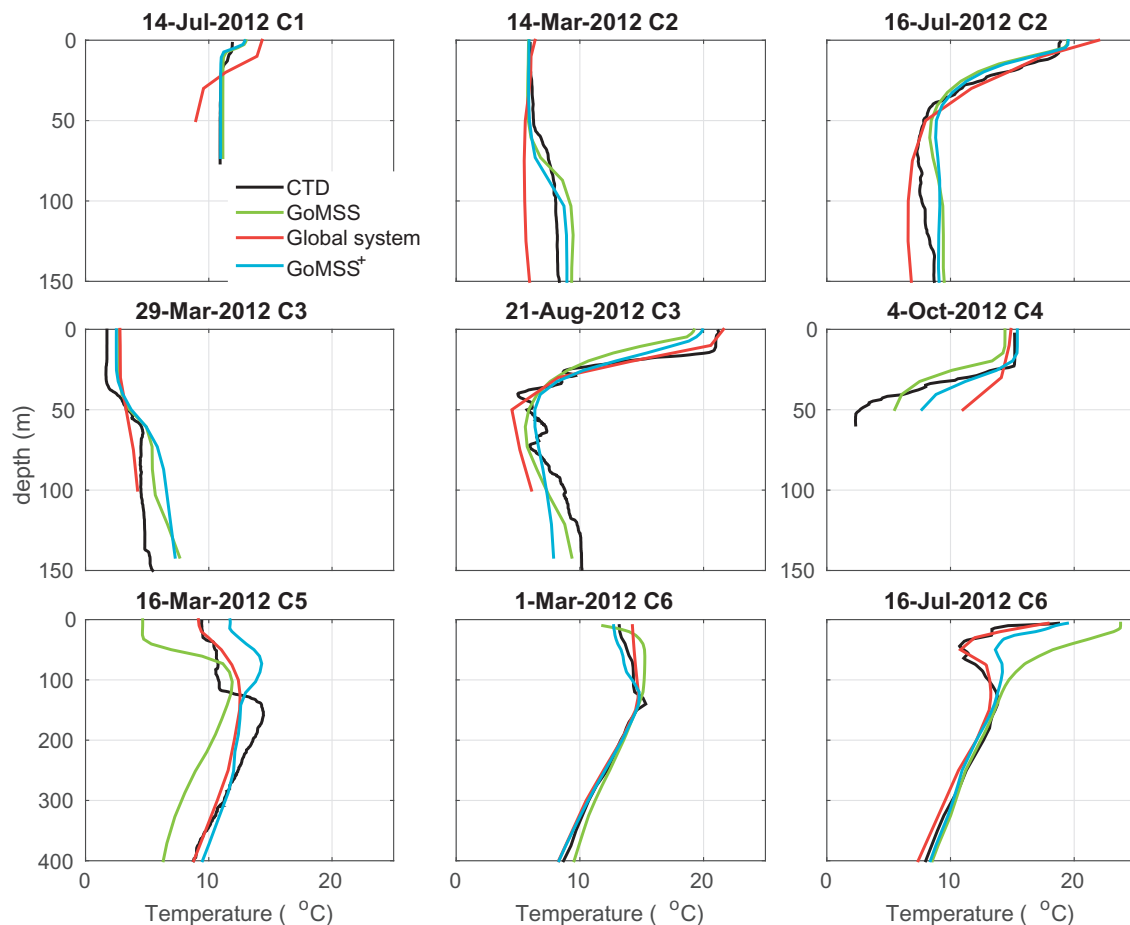


Fig. B1. Representative vertical profiles of temperature from CTD and Argo observations (black) and predictions by the global system (red), GoMSS (green) and GoMSS+ (blue). The six locations of the profiles are shown in Fig. 2 and the dates are given in the title of each subpanel. (For interpretation of the references to colour in this figure legend, the reader is referred to the web version of this article.)

in the present study only nudges low wave-numbers (there is no frequency dependent nudging) and thus is more similar to the method used to downscale atmospheric conditions.

Appendix B. Observed and predicted temperature and salinity profiles

Temperature and salinity profiles predicted by GoMSS, the global system and GoMSS⁺ for six locations (C1 to C6 in Fig. 2) are now discussed. The observed and predicted profiles are shown in Figs. B.1 and B.2. These profiles are representative of the temperature and salinity profiles in the Bay of Fundy, the Gulf of Maine, the Scotian Shelf, the shelf break and the deep water.

Global System: At C1 (Bay of Fundy) the global system overestimates sea surface temperature by about 2°C and underestimates the surface salinity by about 1. It also predicts a sharper and deeper thermocline and halocline than observed. At C2 (Gulf of Maine), within 60 m of the surface the global system predicts well the mixed layer with temperature around 6°C and salinity 32.7, in winter. Below 60 m it underestimates temperature and salinity. In summer, the global system predicts accurately the observed thermocline and halocline at C2. At C3 (Scotian Shelf) the global system reproduces the observed thermocline and halocline shapes during summer. However, in winter it predicts a more uniform temperature profile and overestimates salinity by about 1 throughout the water column. At C4 (north Scotian Shelf), the global system does not capture the observed sharp thermocline and halocline and overestimates surface salinity by about 0.7.

At the shelf break (C5) the global system accurately predicts surface temperature and salinity but generates more uniform profiles than observed. At C6 (deep water) the global system captures well the observed temperature and salinity profiles.

GoMSS: At C1 GoMSS reproduces the shape of the observed salinity and temperature profiles but underestimates surface salinity by about 0.7. At C2 GoMSS predicts temperature profiles consistent with observations during both winter and summer. However, it underestimates salinity for $z < 50$ m and overestimates salinity for $z > 100$ m during winter and summer. At C3 GoMSS reproduces the temperature and salinity profiles shapes but overestimates salinity throughout the water column in winter and underestimates salinity for $z > 50$ m in summer. At C4 GoMSS predicts a realistic thermocline and halocline, but underestimates surface temperature by about 0.7°C.

At the shelf break (C5) GoMSS underestimates surface temperature and salinity by about 5°C and 2.5, respectively, and does not reproduce the overall shape of the profiles. At C6, GoMSS does not reproduce the shape of the observed salinity and temperature profiles. In summer it overestimates temperature and salinity for $z < 100$ m.

GoMSS⁺: At C1 GoMSS⁺ predicts temperature and salinity profiles that are similar to GoMSS and in good agreement with the observations. At C2 it predicts well the observed temperature profiles in winter and summer. However, it generally overestimates salinity. At C3 GoMSS⁺ captures well the temperature profiles and thermocline shape, but overestimates salinity during winter and predicts a more uniform salinity profile during summer. At C4 it provides accurate predictions of the observed temperature and salinity profiles.

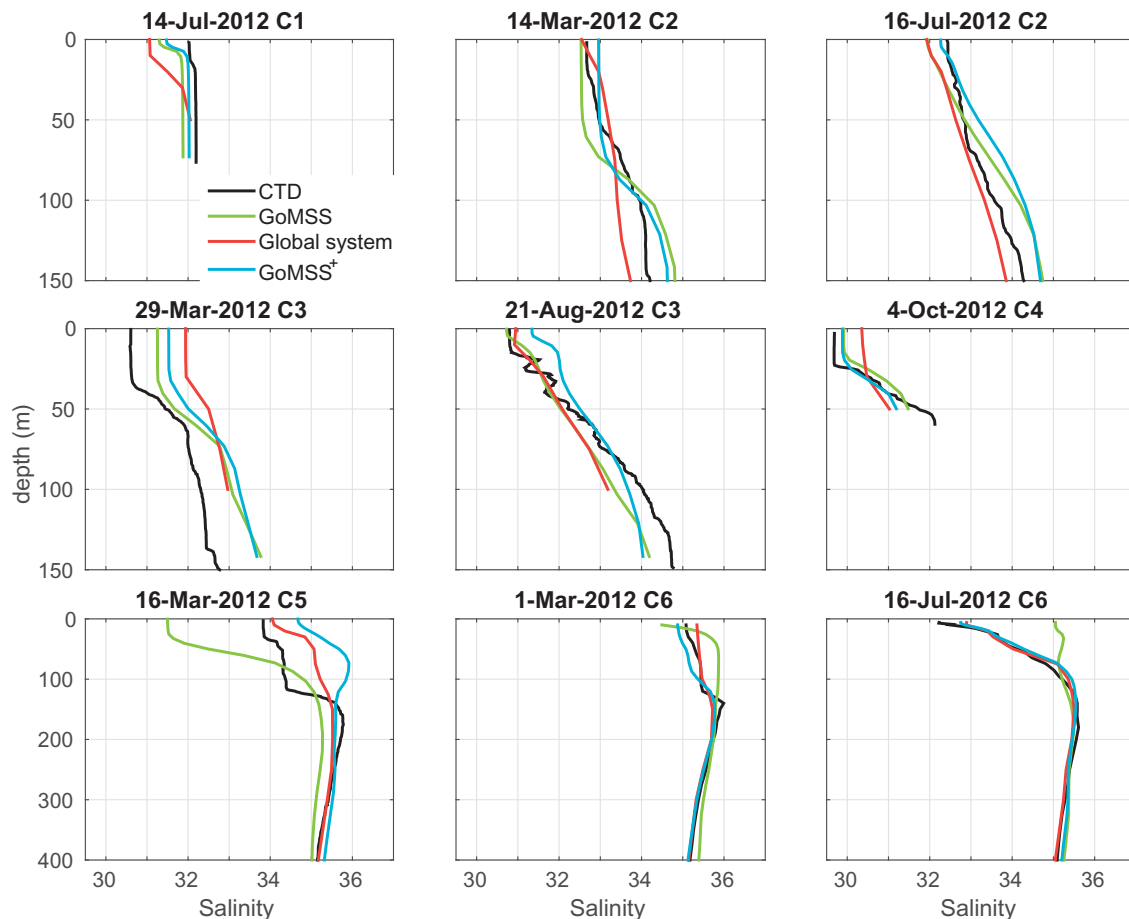


Fig. B.2. Vertical profiles of salinity from CTD and Argo observations (black), and predictions by the global system (red), GoMSS (green) and GoMSS⁺ (blue). Otherwise same format as Fig. B.1. (For interpretation of the references to colour in this figure legend, the reader is referred to the web version of this article.)

At the shelf break (C5) GoMSS+ reproduces the shape of the observed salinity and temperature profiles but overestimates temperature and salinity by about 2°C and 1, respectively, for $z < 100$ m. At C6 it gives accurate predictions of temperature and salinity in both winter and summer.

References

- Alexandru, A., de Elia, R., Laprise, R., Separovic, L., Biner, S., 2009. Sensitivity study of regional climate model simulations to large-scale nudging parameters. *Mon. Wea. Rev.* 137, 1666–1686. <http://dx.doi.org/10.1175/2008MWR2620.1>.
- Allen, S.E., Vindeirinho, C., Thomson, R.E., Foreman, M.G.G., Mackas, D.L., 2001. Physical and biological processes over a submarine canyon during an upwelling event. *Can. J. Fish. Aquat. Sci.* 58, 671–684. doi:10.1139/f01-008.
- Blayo, E., Debret, L., 2006. Nesting ocean models. In: Chassignet, E.P., Verron, J. (Eds.), *An Integrated View of Oceanography: Ocean Weather Forecasting in the 21st Century*. Kluwer.
- Bleck, R., 2002. An oceanic general circulation model framed in hybrid isopycnal-Cartesian coordinates. *Ocean Modell.* 4, 55–88. doi:10.1016/S1463-5003(01)00012-9.
- Boyer, T.P., Antonov, J.I., Baranova, O.K., Coleman, C., Garcia, H.E., Grodsky, A., Johnson, D.R., Locarnini, R.A., Mishonov, A.V., Brien, T.D.O., Paver, C.R., Reagan, J.R., Seidov, D., Smolyar, I.V., Zweng, M.M., 2013. *World Ocean Database 2013*, vol. 72, p. 209.
- Brickman, D., Drozdowski, A., 2012. Development and validation of a regional shelf model for Maritime Canada based on the NEMO-OPA circulation model. *Canadian Technical Report of Hydrography and Ocean Sciences 278*. Bedford Institute of Oceanography, Dartmouth, NS, Canada.
- Brooks, D.A., 1985. Vernal circulation in the Gulf of Maine. *J. Geophys. Res.* 90, 4687–4706. doi:10.1029/JC090iC03p04687.
- Butman, B., Beardsley, R.C., Magnell, B., Frye, D., Vermersch, J.A., Schlitz, R., Limeburner, R., Wright, W.R., Noble, M.A., 1982. Recent observations of the mean circulation on Georges Bank. *J. Phys. Oceanogr.* 12, 569–591. doi:10.1175/1520-0485.
- Capet, X., McWilliams, J.C., Molemaker, M.J., Shchepetkin, A.F., 2008. Mesoscale to submesoscale transition in the California Current system. Part III: energy balance and flux. *J. Phys. Oceanogr.* 38, 2256–2269. <http://dx.doi.org/10.1175/2008JP03810.1>.
- Caya, D., Biner, S., 2004. Internal variability of RCM simulations over an annual cycle. *Climate Dyn.* 22, 33–46. doi:10.1007/s00382-003-0360-2.
- Chassignet, E.P., Hurlburt, H.E., Metzger, E.J., Smedstad, O.M., Cummings, J.A., Halliwell, G.R., Bleck, R., Baraille, R., Wallcraft, A.J., Lozano, C., Tolman, H.L., Srinivasan, A., Hankin, S., Cornillon, P., Weisberg, R., Barth, A., He, R., Werner, F., Wilkin, J., 2009. US GODAE global ocean prediction with the HYbrid Coordinate Ocean Model (HYCOM). *Oceanography* 22, 64–75. doi:10.5670/oceanog.2009.39.
- Chassignet, E.P., Hurlburt, H.E., Smedstad, O.M., Halliwell, G.R., Hogan, P.J., Wallcraft, A.J., Baraille, R., Bleck, R., 2007. The HYCOM (HYbrid Coordinate Ocean Model) data assimilative system. *J. Mar. Syst.* 65, 60–83. doi:10.1016/j.jmarsys.2005.09.016.
- Chen, C., Beardsley, R., Franks, P.J.S., 2001. A 3-D prognostic numerical model study of the Georges Bank ecosystem. part I: physical model. *Deep Sea Res. II* 48, 419–456. doi:10.1016/S0967-0645(00)00124-7.
- Cummings, J.A., 2005. Operational multivariate ocean data assimilation. *Quart. J. Roy. Meteor. Soc.* 131, 3583–3604. doi:10.1256/qj.05.105.
- Cummings, J.A., Smedstad, O.M., 2013. Variational data assimilation for the global ocean. In: Park, S.K., Xu, L. (Eds.), *Data Assimilation for Atmospheric, Oceanic and Hydrologic Applications Vol II*. Springer, pp. 303–343.
- Davies, H.C., 1976. A lateral boundary formulation for multi-level prediction models. *Quart. J. Roy. Meteor. Soc.* 102, 405–418. doi:10.1002/qj.49710243210.
- Denis, B., Laprise, R., Caya, D., Côté, J., 2002. Downscaling ability of one-way nested regional climate models: the big-brother experiment. *Clim. Dyn.* 18, 627–646. doi:10.1007/s00382-001-0201-0.
- de Elia, R., Laprise, R., Denis, B., 2002. Forecasting skill of nested limited-area models: a perfect model approach. *Mon. Wea. Rev.* 130, 2006–2023. [http://dx.doi.org/10.1175/1520-0493\(2002\)130\(2006:FSLONL\)2.0.CO;2](http://dx.doi.org/10.1175/1520-0493(2002)130(2006:FSLONL)2.0.CO;2)
- Ferrari, R., Wunsch, C., 2009. Ocean circulation kinetic energy: reservoirs, sources and sinks. *Annu. Rev. Fluid Mech.* 41, 253–282. doi:10.1146/annurev.fluid.40.111406.102139.
- Flather, R.A., 1976. A tidal model of the northwest European continental shelf. *Mem. Soc. R. Sci. Liege* 10, 141–164.
- Fox, D.N., Teague, W.J., Barron, C.N., Carnes, M.R., Lee, C.M., 2002. The Modular Ocean Data Assimilation System (MODAS). *J. Atmos. Oceanic Technol.* 19, 240–252. [http://dx.doi.org/10.1175/1520-0426\(2002\)019\(0240:TMODAS\)2.0.CO;2](http://dx.doi.org/10.1175/1520-0426(2002)019(0240:TMODAS)2.0.CO;2)
- Giorgi, F., Bi, X., 2000. A study of internal variability of a regional climate model. *J. Geophys. Res.* 105, 29503–29521. doi:10.1029/2000JD900269.
- Greenberg, D.A., 1983. Modelling the mean barotropic circulation in the Bay of Fundy and Gulf of Maine. *J. Phys. Oceanogr.* 13, 886–904. doi:10.1175/1520-0485(1983)013(0886:MTMBCI)2.0.CO;2.
- Han, G., Hannah, C.G., Loder, J.W., Smith, P.C., 1997. Seasonal variation of the three-dimensional mean circulation over the Scotian Shelf. *J. Geophys. Res.* 102, 1011–1025. doi:10.1029/96JC03285.
- Han, G., Roussel, P., Loder, J.W., 2001. Modeling tidal currents and seasonal-mean circulation in the Sable Gully region. In: *Estuarine and Coastal Modeling: Proceedings of the seventh International ASCE Conference*. American Society of Civil Engineers, Petersburg, FL, pp. 22–34.
- Hannah, C.G., Shore, J.A., Loder, J.W., Naimie, C.E., 2001. Seasonal circulation on the western and central Scotian Shelf. *J. Phys. Oceanogr.* 31, 591–615. doi:10.1175/1520-0485(2001)031(0591:SCOTWA)2.0.CO;2.
- Henshaw, W., Kreiss, H., Ystrom, J., 2003. Numerical experiments on the interaction between the large- and small-scale motions of the Navier–Stokes equations. *Multiscale Model. Simul.* 1, 119–149. doi:10.1137/S1540345902406240.
- Katavouta, A., Thompson, K.R., 2013. Downscaling ocean conditions: experiments with a quasi-geostrophic model. *Ocean Modell.* 72, 231–241. doi:10.1016/j.oceomod.2013.10.001.
- Katavouta, A., Thompson, K.R., Lu, Y., Loder, J.W., 2015. Interaction between the tidal and seasonal variability of the Gulf of Maine and Scotian Shelf region. submitted to *J. Phys. Oceanogr.*
- Laprise, R., 2003. Resolved scales and nonlinear interactions in limited-area models. *J. Atmos. Sci.* 60, 768–779. [http://dx.doi.org/10.1175/1520-0469\(2003\)060\(0768:RSANII\)2.0.CO;2](http://dx.doi.org/10.1175/1520-0469(2003)060(0768:RSANII)2.0.CO;2)
- Laprise, R., Kornic, D., Rapaic, M., Separovic, L., Leduc, M., Nikiema, O., Luca, A.D., Diaconescu, E., Alexandru, A., Lucas-Picher, P., de Elia, R., Caya, D., Biner, S., 2012. Considerations of domain size and large-scale driving for nested regional climate models: impact on internal variability and ability at developing small-scale details. In: Berger, A., Mesinger, F., Sijacki, D. (Eds.), *Climate Change: Inferences from Paleoclimate and Regional Aspects*. Springer, Heidelberg.
- LeTraon, P.Y., Klein, P., Hua, B.L., Dibarboure, G., 2008. Do altimeter wavenumber spectra agree with the interior of surface quasigeostrophic theory? *J. Phys. Oceanogr.* 38, 1137–1142. <http://dx.doi.org/10.1175/2007JP03806.1>.
- Loder, J.W., 1980. Topographic rectification of tidal currents on the sides of Georges Bank. *J. Phys. Oceanogr.* 10, 1399–1416. doi:10.1175/1520-0485(1980)010(1399:TROTCO)2.0.CO;2.
- Loder, J.W., Hannah, C.G., Petrie, B.D., Gonzalez, E.A., 2003. Hydrographic and transport variability on the Halifax section. *J. Geophys. Res.* 108. doi:10.1029/2001JC001267.
- Loder, J.W., Petrie, B., Gawarkiewicz, G., 1998. Chapter 5, the coastal ocean off north-eastern North America: a large-scale view. In: Robinson, A.R., Brink, K.H. (Eds.), *The Sea*, 11. John Wiley and Sons, Inc., pp. 105–133.
- Loder, J.W., Wright, D.G., 1985. A depth-dependent study of the topographic rectification of tidal currents. *Geophys. Astrophys. Fluid Dyn.* 31, 169–220. doi:10.1080/03091928508219269.
- Lyard, F., Lefevre, F., Letellier, T., Francis, O., 2006. Modelling the global ocean tides: modern insight from FES2004. *Ocean Dyn.* 56, 394–415. doi:10.1007/s10236-006-0086-x.
- Lynch, D.R., Ip, J.T.C., Naimie, C.E., Werner, F.E., 1996. Comprehensive coastal circulation model with application to the Gulf of Maine. *Cont. Shelf Res.* 16, 875–906. doi:10.1016/0278-4343(95)00028-3.
- Madec, G., 2008. NEMO ocean engine. *Note du Pole de modélisation 27* ISSN. Institut Pierre-Simon Laplace (IPSL), France.
- Madec, G., Delecluse, P., Imbard, M., Levy, C., 1998. OPA8.1 Ocean general Circulation Model reference manual. *Note du Pole de modélisation 11*. Institut Pierre-Simon Laplace (IPSL), France.
- Marchesio, P., McWilliams, J.C., Shchepetkin, A., 2001. Open boundary conditions for long-term integration of regional oceanic models. *Ocean Modell.* 3, 1–20. doi:10.1016/S1463-5003(00)00013-5.
- Metzger, E.J., Hurlburt, H.E., Wallcraft, A.J., Shriver, J.F., Smedstad, L.F., 2008. Validation Test Report for the Global Ocean Prediction System V3.0-1/12. HYCOM/NCODA: Phase I. Memorandum Report. Naval Research Laboratory, Stennis Space Center.
- Molins, J.M., Barnier, B., Penduff, T., Treguier, A.M., Sommer, J.L., 2014. ORCA12.L46 climatological and interannual simulations forced with DFS4.4: GJM02 and MJM88. Drakkar Group Experiment report GDRI-DRAKKAR-2014-03-19. LGGE-Grenoble, LPO, France.
- Naimie, C.E., Loder, J.W., Lynch, D.R., 1994. Seasonal variation of the three-dimensional residual circulation on Georges Bank. *J. Geophys. Res.* 99, 15967–15989. doi:10.1029/94JC01202.
- Nutter, P., Stensrud, D., Xue, M., 2004. Effects of coarsely resolved and temporally interpolated lateral boundary conditions on the dispersion of limited-area ensemble forecasts. *Mon. Wea. Rev.* 132, 2358–2377. [http://dx.doi.org/10.1175/1520-0493\(2004\)132\(2358:EOCRAT\)2.0.CO;2](http://dx.doi.org/10.1175/1520-0493(2004)132(2358:EOCRAT)2.0.CO;2)
- Rhines, P.B., 1975. Waves and turbulence on a beta-plane. *J. Fluid Mech.* 69, 417–443. doi:10.1017/S0022112075001504.
- Rinke, A., Marbaix, P., Dethloff, K., 2004. Internal variability in Arctic regional climate simulations: case study of SHEBA year. *Climate Res.* 27, 197–209. doi:10.3354/cr027197.
- Roblou, L., Lamouroux, J., Bouffard, J., Lyard, F., Hénaff, M.L., Lombard, A., Marsaleix, P., Mey, P.D., Birol, F., 2011. Chapter 9: Post-processing altimeter data towards coastal applications and integration into coastal models. In: Vignudelli, S., Kostianoy, A.G., Cipollini, P., Benveniste, J. (Eds.), *Coastal Altimetry*. Springer.
- Saha, S., Moorthi, S., Pan, H.-L., Wu, X., Wang, J., Nadiqa, S., Trpp, P., Kistler, R., Woollen, J., Behringer, D., Liu, H., Stokes, D., Grumbine, R., Cayno, G., Wang, J., Hou, Y.-T., Chuang, H.-Y., Juang, H.-M.H., Sela, J., Iredell, M., Treadon, R., Kleist, D., Delst, P.V., Keyser, D., Derber, J., Ek, M., Meng, J., Wei, H., Yang, R., Lord, S., Dool, H.V.D., Kumar, A., Wang, W., Long, C., Chelliah, M., Xue, Y., Huang, B., Schemm, J.-K., Ebisuzaki, W., Lin, R., Xie, P., Chen, M., Zhou, S., Higgins, W., Zou, C.-Z., Liu, Q., Chen, Y., Han, Y., Cucurull, L., Reynolds, R.W., Rutledge, G., Goldberg, M., 2010. The NCEP climate forecast system reanalysis. *Bull. Amer. Meteor. Soc.* 91, 1015–1057. doi:10.1175/2010BAMS3001.1.

- Shan, S., Sheng, J., Greenan, B.J.W., 2014. Physical processes affecting circulation and hydrography in the Sable Gully of Nova Scotia. *Deep Sea Res. II* 104, 35–50. doi:[10.1016/j.dsr2.2013.06.019](https://doi.org/10.1016/j.dsr2.2013.06.019).
- Smith, P.C., 1983. The mean and seasonal circulation off southwest Nova Scotia. *J. Phys. Oceanogr* 13, 1034–1054. doi:[10.1175/1520-0485\(1983\)013\(1034:TMASCO\)2.0.CO;2](https://doi.org/10.1175/1520-0485(1983)013(1034:TMASCO)2.0.CO;2).
- von Storch, H., Langenberg, H., Feser, F., 2000. A spectral nudging technique for dynamical downscaling purposes. *Mon. Wea. Rev.* 128, 3664–3673. [http://dx.doi.org/10.1175/1520-0493\(2000\)128\(3664:ASNTFD\)2.0.CO;2](http://dx.doi.org/10.1175/1520-0493(2000)128(3664:ASNTFD)2.0.CO;2)
- Taylor, K.E., 2001. Summarizing multiple aspects of model performance in a single diagram. *J. Geophys. Res.* 106, 7182–7192. doi:[10.1029/2000JD900719](https://doi.org/10.1029/2000JD900719).
- Thompson, K.R., Wright, D.G., Lu, Y., Demirov, E., 2006. A simple method for reducing seasonal bias and drift in eddy resolving ocean models. *Ocean Modell.* 13, 109–125. doi:[10.1016/j.ocemod.2005.11.003](https://doi.org/10.1016/j.ocemod.2005.11.003).
- Urrego-Blanco, J., Sheng, J., 2014. Study on subtidal circulation and variability in the Gulf of St. Lawrence, Scotian Shelf, and Gulf of Maine using a nested-grid shelf circulation model. *Ocean Dyn.* 64, 385–412. doi:[10.1007/s10236-013-0688-z](https://doi.org/10.1007/s10236-013-0688-z).
- Vallis, G.K., 2006. *Atmospheric and Oceanic Fluid Dynamics*. Cambridge University Press, Cambridge, U.K.
- Waldron, K.M., Peagle, J., Horel, J.D., 1996. Sensitivity of a spectral filtered and nudged limited-area model to outer model options. *Mon. Wea. Rev.* 124, 529–547. [http://dx.doi.org/10.1175/1520-0493\(1996\)124\(0529:SOASFA\)2.0.CO;2](http://dx.doi.org/10.1175/1520-0493(1996)124(0529:SOASFA)2.0.CO;2)
- Wright, D.G., Thompson, K.R., Lu, Y., 2006. Assimilating long term hydrographic information into an eddy permitting model of the north atlantic. *J. Geophys. Res.* 111, (C09022). doi:[10.1029/2005JC003200](https://doi.org/10.1029/2005JC003200).